DEGREE PROJECT IN TECHNOLOGY,
SECOND CYCLE, 30 CREDITS
STOCKHOLM, SWEDEN 2022

SSRT of 10-4 FeCrAl in LBE and Pb to characterize LME effects

KTH Master Thesis Report

Daniel Stein

KTH ROYAL INSTITUTE OF TECHNOLOGY
NUCLEAR ENERGY ENGINEERING
TRITA: TRITA-SCI-GRU 2022:045

Authors

Daniel Stein <ddstein@kth.se>
Nuclear Energy Engineering
KTH Royal Institute of Technology

Place for Project

Stockholm, Sweden
Division of Surface Chemistry and Corrosion Science
KTH Royal Institute of Technology

Examiner

Janne Wallenius
Nuclear Engineering
KTH Royal Institute of Technology

Supervisor

Peter Szakalos

Division of Surface Chemistry and Corrosion Science

KTH Royal Institute of Technology

Abstract

In this work the susceptibility of Fe-10Cr-4Al steel to liquid metal embitterment (LME) in low oxygen environment was investigated. slow strain rate testing (SSRT) were conducted on 10-4 FeCrAl steel in a stagnant lead from 340-480°C, lead-bismuth eutectic (LBE) from 140-450°C and lead-bismuth mixture at 375°C with increasing bismuth content from 0.1wt%-40wt%. The results showed that in the stagnant lead environment the FeCrAl steel showed no sign of LME with all samples being subjected to around 25% strain before final break. In LBE the samples were affected by LME especially at 350-400°C. The total elongation to failure reduced in LBE from 25% to 13.1% and a ductility trough from 190-400°C was observed. In the lead-bismuth mixture there was a reduction in ductility at 5wt% going from 25% to 20% total elongation, at 15wt% going from 20% to 16% total elongation and at 30wt% going from 16% to 13% total elongation.

Keywords

Liquid Metal Embrittlement, Lead, Bismuth, Lead-Bismuth Eutectic, Slow Strain Rate Testing

Abstract

I det här arbetet har stålet Fe-10Cr-4Al känslighet till liquidmetal embrittlemnt(LME) i låga syre miljöer av flytande bly, mellan 340-480 °C, och Bly/Vismut eutektisk (LBE), mellan 140-450 °C, undersökts. En stegvis ökning av Vismut halten i flytande bly genfördes också från 0.1 wt% Bi till 40 wt% Bi med en fast temperatur på 375 °C. Resultaten från dessa experiment visade att i ren bly miljö så visade stålet Fe-10Cr-4Al inga tecken på LME, alla prover gick till brott runt 25% strain. I LBE blev stålet svårt på verkat av LME, framför allt inom temperaturer intervallet 350-400 °C. Den totala förlängningen av proverna blev här reducerat från 25% ner till 13.1% och en klar duktilitets tråg mellan 190-400 °C kunde observeras. I experimenten med gradvis ökande Vismut halt observerades markanta nedgångar i stålets duktilitet vid 5 wt% Bi då den droppar från 25% till 20% förlängning, nästa dropp observerades vid 15 wt% Bi, 20%-16% och vid 30 wt% Bi med ett reduktion från 16% till 13%.

Acknowledgements

I would like to express my deepest appreciation for my supervisor Peter Szakalos for his guidance and mentorship throughout the whole endeavor of the project. Even though I arrived at the start of the project with very little knowledge about the topic or material science Peter was very supportive through every step of the process. I would also like to thank Christopher Petersson for the excellent environment that we had in the lab, for the productive discussions and the less so productive discussions.

Most of all I would like to thank Janne Wallenius, you have provided me with so much knowledge through my two years of studies here at KTH. Although we do not agree completely on every aspect you have provided me with so much perspective on the nuclear industry and beyond.

Lastly, I would like to acknowledge the Sauna Squad and all my other friends and family throughout the world, I would not be here today without your undying support and love.

Acronyms

AFA	alumina forming austenite
BCC	body-centered cubic
CSP	concentrated solar power
DPA	displacement per atom
EDS	energy dispersion spectroscopy
FCC	face-centered cubic
GHG	greenhouse gas
HTGR	high-temperature gas-cooled reactor
LBE	lead-bismuth eutectic
LEDC	less economically developed countries
LFR	lead fast reactor
LME	liquid metal embitterment
LWR	light water reactor
MA	minor actinides
MEDC	more economically developed countries
SEM	scanning electron microscopy
SFR	sodium fast reactor
SMR	small modular reactor
SSRT	slow strain rate testing
TEM	transmission electron microscopy
YS	yield strength
UTS	ultimate tensile strength

Contents

Chapter 1

Introduction

1.1 Aim and Scope

The project aimed to investigate and characterize the LME phenomenon of Fe-10Cr-4Al in a liquid lead and LBE environment. FeCrAl is a novel steel that has very promising corrosion-resistant properties in a liquid lead environment allowing it to be used in high-temperature energy applications such as a lead fast reactor (LFR), concentrated solar power (CSP), and thermal storage. The work primarily focuses on the SSRT of FeCrAl to characterize the fracture mode of the steel at different temperatures and environmental conditions.

1.2 Energy Status

The race to net-zero by 2050 has begun with a majority of nations globally announcing at the COP 26 conference a reinforced effort to reduce greenhouse gas (GHG) emissions by the end of the decade [1]. The current GHG emissions represented as carbon dioxide equivalents with respect to the sector are presented in Figure 1.2.1. The energy sector is responsible for the majority of the GHG, accounting for nearly 76% or 37.22 Gt CO_2 equivalents.

Furthermore, the majority of the increase in GHG emissions since the 1980's can be accounted for by the energy sector. The energy sector can be broken down further into sub-sectors, including electricity and heat production. The evolution of the percentage contribution of each sub-sector is given in Figure 1.2.2. The electricity and

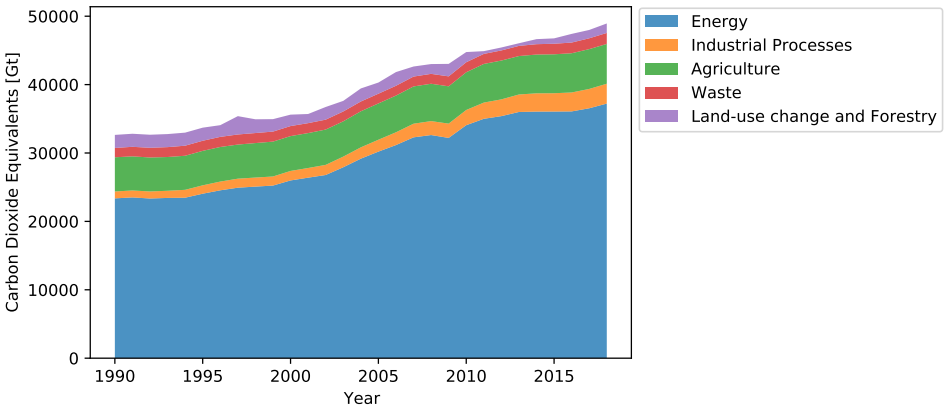

Figure 1.2.1: Carbon dioxide equivalents emitted by sector [2]

heat production sector has shown the most significant growth, from 37% in 1980 to 42% in 2018 or a nominal emission of 15.59 CO_2e. This means that nearly one-third of the global GHG emissions are from electricity and heat production and currently growing year over year [2]. For nations to maintain the goals presented at the COP 26 conference, a major reduction of GHG emissions in the electricity production needs to be achieved. The current method of achieving such a goal is for more economically developed countries (MEDC) to phase out coal plants by 2030 and for less economically developed countries (LEDC) to phase out coal plants by 2040 [1]. This will leave a gap in energy production that needs to be compensated by either rapid expansion of renewable sources coupled with viable energy storage options such as thermal storage or by expanding nuclear energy as a baseload power source.

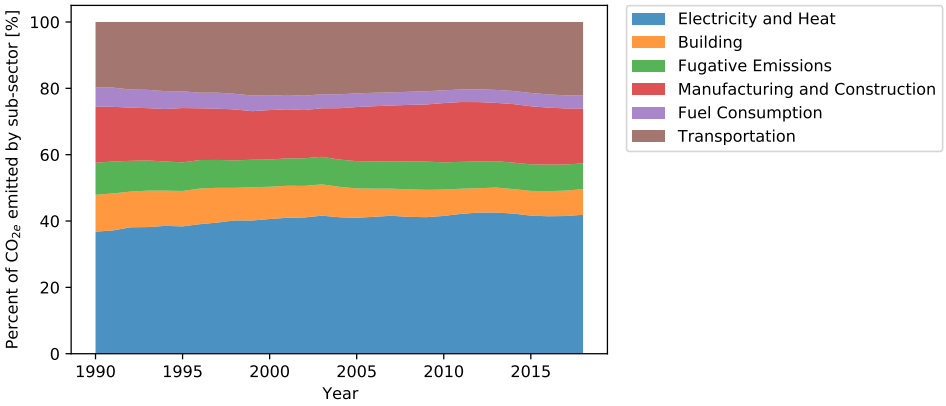

Figure 1.2.2: Percentage of carbon dioxide equivalents emitted by energy sub-sector [2]

1.3 Nuclear Energy

There are around 440 operational second and third-generation commercial nuclear power plants globally, which produce approximately 2,553 TWh accounting for 10% of global electricity production [3]. The current reactor designs are water-cooled and water-moderated known as light water reactor (LWR). Neutrons in these reactor designs are in the thermal spectrum as the hydrogen atoms in the water effectively reduce the neutron energy through collision processes. In the thermal spectrum, the neutron cross-sections of both scattering and fission events are significantly larger, allowing for low enrichment levels of the nuclear fuel [4]. Due to this low enrichment and wide availability of water, this technology became widely commercialized in the 1960's and 70's.

Data indicates that nuclear power is among the lowest carbon emitter, emitting nearly 100 times less carbon dioxide equivalents than coal and over half as much as solar power in direct and indirect GHG emissions, as shown in figure 1.3.1 [5]. This makes nuclear power a prime candidate for nations attempting to maintain net-zero goals posed at the COP 26 conference.

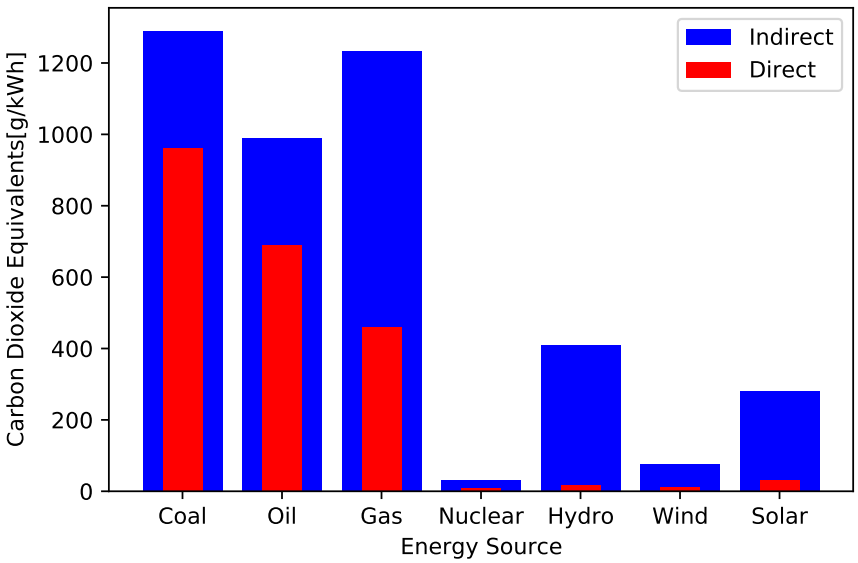

Figure 1.3.1: Carbon dioxide equivalents emissions of energy sources [5]

Apart from being the lowest GHG emitter of the major energy sources, nuclear power is also one of the safest. Despite accidents that have defined the public perception of nuclear – such as Three Mile Island, Chernobyl, and Fukushima Daiichi – deaths

resulting from these accidents and resultant pollution are significantly lower than that of fossil fuels and on the same order of magnitude as the renewable sources depicted in figure 1.3.2 [6]. Although nuclear energy has these advantages in an ecological and health regard, there are legitimate concerns, especially regarding the waste produced from the LWRs. The radiotoxicity and decay heat of the spent fuel can be differentiated into two major components, that of the fission products – including ^{137}Cs, ^{90}Sr,^{131}I among other – and that of the minor actinides (MA) – including ^{241}Am and ^{244}Cm. The fission products' decay heat and radiotoxicity diminish to near-zero values after about 300 years, whereas the MA would need to be stored for time periods up to 100,000 years to ensure the reduction of the decay heat and radiotoxicity to levels lower than natural uranium [7].

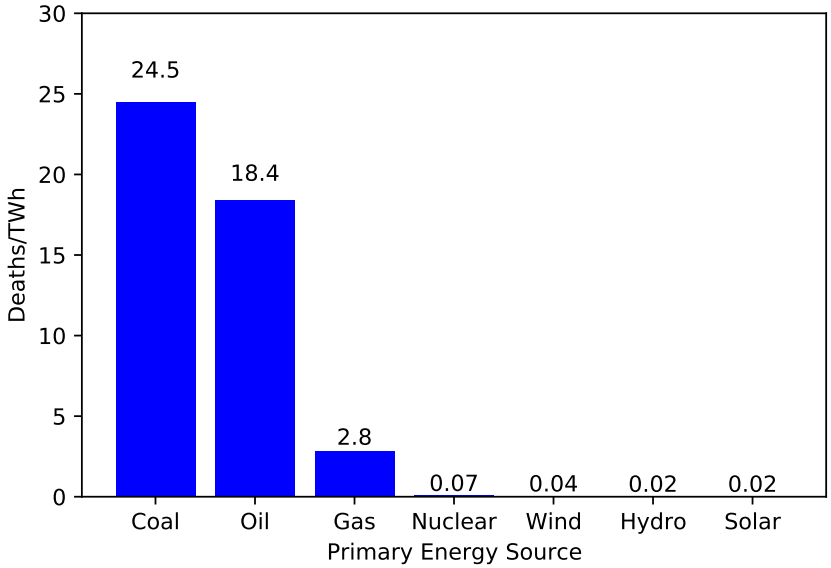

Figure 1.3.2: Deaths caused by accidents and pollution related illnesses [6]

1.4 The Fourth Generation

The fourth generation of nuclear power plants, also called Gen IV, aims at addressing the issue of long-lived MA specifically. The four main goals of the Gen IV concept are [8]:

- Sustainability

  Providing energy that meets clean air objectives while achieving long-term availability of systems

Minimizing and managing nuclear waste

- Economics

  Life cycle cost advantage and comparable economic risk to other energy sources

- Safety and Reliability

  Excel in safety and reliability with a very low probability of core damage eliminating the need for off-site emergency response

- Proliferation Resistance

  Gen IV systems will create the least desirable route for the diversion or theft of weapon-grade material

While this is not a necessity, many of the Gen IV designs are fast reactors meaning that there is no moderator to slow the neutrons into the thermal spectrum. This has the consequence that while the overall neutron cross-sections for capture and fission decrease, the fission-to-capture ratio increases [9]. Two main effects can be drawn from this, firstly, a larger enrichment value will be needed to maintain a critical mass for the fission chain reaction. Secondly, fewer long-lived MA will be produced as fission of the actinide atoms has a significantly higher probability relative to neutron capture. The current most widely researched reactor designs are the high-temperature gas-cooled reactor (HTGR) – selected as the UK demonstrator of the Gen IV concept in December 2021 [10] – the sodium fast reactor (SFR) – selected to be the US demonstrator of the Gen IV concept in October 2021 [11] – and the LFR – a joint venture between Uniper, Leadcold, and KTH aim to bring lead cooled small modular reactor (SMR)s to the Swedish energy market [12]. These reactor types use gas, sodium and lead, respectively, as coolant each of which is an ineffective moderator resulting in a fast spectrum design. The LFR has some intrinsic advantages as a reactor design compared to the alternatives of the SFR and HTGR, namely the large density difference across temperatures. This allows for a natural circulation regimen to govern decay heat removal. This means that in the event of an unprotected loss of flow, natural circulation will still remove enough heat for the fuel not to reach its melting point. Additionally, there are radiological advantages since ^{131}I and ^{137}Cs have a strong affinity to lead and therefore will not volatilize in the event of a severe accident reducing the source term of the reactor. Furthermore, lead acts as a gamma radiation shield protecting workers,

reducing concrete requirements [13]. LBE has been considered as a coolant for nuclear power plants as well and provides similar advantages to lead, while also giving the further advantage of a lower melting temperature. Since, the maximum temperature currently limited by steel corrosion resistance of the steel at around 400°C. This widens the possibility for the operating temperature of the nuclear reactor improving the overall efficiency. Additionally the high melting point of the lead coolant means that the water in the steam generator must exceed 327°C at all times to prevent freezing issues of the lead in the steam generator. This is achieved by the addition of a steam generator inlet heater, this increases the internal energy consumption which decreases the overall efficiency of the nuclear power plant [14]. However, the use of LBE in a nuclear reactor also poses some challenges and potential threats. The first of these issues is the formation of nickel-bismuth intermetallic compounds, which can lead to blockages in the primary system of the nuclear reactor [15]. The activation of bismuth in the neutron flux of the core is also an issue that must be considered. Due to a neutron capture reaction described in equation 1.1:

$$^{209}\mathrm{Bi} + n = {}^{210}\mathrm{Po} \tag{1.1}$$

where N is the neutron. It is estimated that the primary circuit of a LBE cooled will be contaminated by about 0.1ppm of highly radioactive ^{210}Po. This quantity of polonium accounts for the largest contributing factor to the source term of a LBE cooled reactor [16].

1.5 Liquid Lead Energy Application

Beyond the LFR, liquid lead has multiple other potential energy applications, including CSP and thermal energy storage systems. In all three cases, the fundamental properties of lead of the high boiling point, high heat transfer, and high thermal capacity make it an excellent candidate for these applications [17]. Due to these properties, lead can effectively be heated either by removing heat from the active core in the LFR or by heating from CSP. Additionally, the high capacity allows for the potential storage of a large amount of thermal energy in liquid lead. The high temperature of the lead environment does pose some challenges. Specifically corrosion of steels at elevated temperature (>400°C) rapidly increases as the kinetics of the chemical reaction increases. However, at lower temperatures (<400°C), a phenomenon known

as LME weakens the structural materials causing premature failure in the structural materials.

Chapter 2

Theory and Background

2.1 Alumina Forming Steel Alloys

Conventional stainless steel have >10% Chromium by weight in the composition, which forms the protective oxide chromia (Cr_2O_3) layer responsible for the passivisation of the steel increasing its corrosive-resistance [18]. In contrast, a relatively new form of corrosion-resistant steel is the alumina (Al_2O_3) forming stainless steel, have demonstrated better corrosion properties compared to conventional chromia forming alloys [19]. This is attributed to the high chemical inertia, a property defined as a materials ability to resist the chemical influence of gasses and liquids in the chemical environment, and low diffusion coefficient, which results in very thin alumina layers on the steel [20, 21]. In this section, two primary alumina forming stainless steels will be discussed in the form of the austenite and ferrite.

2.1.1 Alumina forming austenite

The academic and industrial interest in alumina forming austenite (AFA) steels has grown in recent years following successful work at Oak Ridge National Laboratory, have demonstrated excellent thermal creep resistance in a temperature range of 600-900°C [22], and corrosion resistance in dry and humid air [23], all for the eventual use of high-temperature processes [24]. A long-term corrosion study of austenitic steels was carried out in liquid lead at KTH [25]. It was found that chromia forming austenitic steel such as 316L suffered from either continuous dissolution of nickel to a depth of 300 μm or as in 15-15Ti which had local dissolution of nickel to a depth of 20-50 μm.

AFA steels with varying nickel contents were tested. The AFA steel containing 20 wt% nickel did not show any corrosion beyond 10-20 μm, while the 14 weight percent did not show any dissolution attack. The major issue with the dissolution of nickel in the austenitic steel is the possibility of a phase transition. Iron at room temperature has a body-centered cubic (BCC) crystal structure, whereas nickel has a face-centered cubic (FCC) crystal structure. The crystal structure of austenitic steel is FCC which means that nickel acts as a stabilizer to the austenitic phase. The dissolution of nickel causes a phase transition to occur where austenitic steel transitions into ferritic steel. The ferritic steel is known to generally have weaker mechanical proprieties at the interested temperature range of an LFR.

2.1.2 FeCrAl

The FeCrAl stainless steel has a less densely packed BCC crystal structure relative to the FCC crystal structure of the AFA. The early FeCrAl steel developed by Hans von Kantzow, who later was the founder of Kanthal. The early development of FeCrAl was a simple addition of chromium to the already existing FeAl steel. The high aluminum content made the steel brittle and difficult to manufacture [26, 27]. The addition of chromium is an example of the wider phenomenon known as the third element effect, which allows for a significant reduction in the atomic percentage of aluminum in the alloyed steel. As the aluminum oxidizes to alumina at the surface, the aluminum becomes depleted. In a FeAl alloy, this depleted zone near the surface would eventually cause the alumina scale on the surface to break down as aluminum would no longer be available for the oxidation reaction. The addition of chromium increases the diffusion of aluminum to the surface as the surface will be slightly Cr-depleted since the chromia formation is kinetically faster than that of alumina. However, the diffusion of chromium from the bulk is significantly slower than that of aluminum. This means that aluminum will diffuse from the bulk to the surface to a high enough concentration of aluminum to maintain the alumina scale on the surface of the metal [27].
In a recent collaboration between Sandvik subsidiary Kanthal and KTH, an accelerated effort to develop the FeCrAl with the following weight percent composition presented in table 2.1.1 [28–30].

The reactive elements denoted in the table as RE, are a group of elements that have a high affinity to oxygen, nitrogen or carbon, such as yttrium, titanium, zirconium,

Table 2.1.1: FeCrAl weight percent composition

Elements	Fe	Cr	Al	RE
Weight percent	Balance	10	4	< 1

hafnium, niobium, and thorium. In the FeCrAl developed by Kanthal the reactive elements are an optimized blend of titanium, zirconium, and niobium. While there is no consensus on the mechanism, the reactive elements improve oxidation properties. In alumina-forming steels such as FeCrAl specifically, an important aspect of the effect of the reactive elements is an increase of the spallation resistance by improving the alumina scale adhesion to the alloy surface [31]. Newer studies have also demonstrated an increase in selective oxidation of aluminum and a reduction of scale growth rate. However, this effect is only noticeable at higher temperatures (>900 °C), allowing for a significant decrease in the aluminum content of the lean FeCrAl. The diffusion of aluminum to the surface is promoted by a decrease in alloy grain sizes and an increase in sub-grain boundaries, which are promoted by the presence of the reactive elements, and their oxide, carbide, and nitride counterparts. Therefore, there is a higher atomic diffusion of aluminum to the surface area of the metal to replenish the aluminum that is depleted in alumina formation [32]. The behavior of the reactive elements in the FeCrAl steel means that the steel can be produced as a lean alloy, meaning a low-weight percent of both aluminum and chromium. The low chromium content is of major significance as an α-α' phase separation, where a chromium-rich phase separates from a iron-rich phase, is unlikely to occur. The new FeCrAl alloys have demonstrated that a α-α' phase separation does not occur while maintaining good ductile characteristics and strong oxidation-resistant properties [28–30, 33].

2.2 Corrosion of Steel in Liquid Lead Environment

Corrosion is the gradual degradation of material into more chemically favorable states by electro-chemical processes involving a redox reaction with the environment. Corrosion of metals can be localized in certain areas. For instance, in crevice corrosion, particularly susceptible are welds and overlapping edges [34], or pitting corrosion, where damage in the protective oxide allow direct contact with the metal and the oxidizing environment [35]. This highly localized form of corrosion can form cracks that propagate through the bulk of the metal, leading to premature failure of the metal

under stress. Corrosion can also be spread over the entire metal surface, referred to as uniform corrosion. This form of corrosion is much easier to detect and prevent [36]. While corrosion in aqueous environments is controlled by electrochemical processes as described above, in liquid metal environments, the corrosion is controlled by a physical or physical-chemical process [37]. One of the primary dissolution issues is the solubility of nickel, which increases from 0.53 at% at 372 °C to 18.63 at% at 1200 °C [38]. With nickel as the austenitic stabilizing element, and austenite steels necessary for their strong mechanical and thermal creep resistant properties, especially in fuel pins and heat exchangers in an LFR, the dissolution of nickel poses a significant threat to the structural integrity of these components. This is demonstrated by the fact that the rate of nickel dissolution is accelerated by the content of nickel in the alloy, as demonstrated in figure 2.2.1. Furthermore, this trend is propagated in LBE,where there is a further linear correlation between the corrosion rate and the bismuth content in the lead. The addition of specific metals, such as titanium or zirconium, in the lead or LBE melt, have demonstrated to mitigate some corrosion effects by reacting with nitrogen from the steel to form TiN or ZrN on the surface of the steel acting as a protective layer. Non-metallic additions to the melt, such as oxygen, have proven to also strongly reduce the effect of corrosion by forming metal oxide layers on the surface of the steel [37].

2.2.1 Oxidation at high temperature

The oxidation reaction is a process where an anode donates electrons to the cathode counterpart in the environment. In liquid metal environments with high oxygen activity in the liquid metal, certain elements in steel, such as chromium and aluminum, will act as the anode and oxygen as the cathode to form an oxide as follows [39]:

$$xM + \frac{y}{2}O_2 \rightarrow M_xO_y \tag{2.1}$$

where M is the metallic species being oxidized and O is oxygen. The oxide layer is a significant inhibitor to corrosion of the steel in the liquid metal environment, therefore to be able to relate the formation energy of the oxide layer to the activity of the oxygen in the lead, it is necessary to predict the oxide formation. The relationship is given as follows:

$$\Delta_f G^{\circ}_{M_xO_y} = -RT * ln\frac{a_{M_xO_y}}{a_M^x * a_O^{y/2}} \tag{2.2}$$

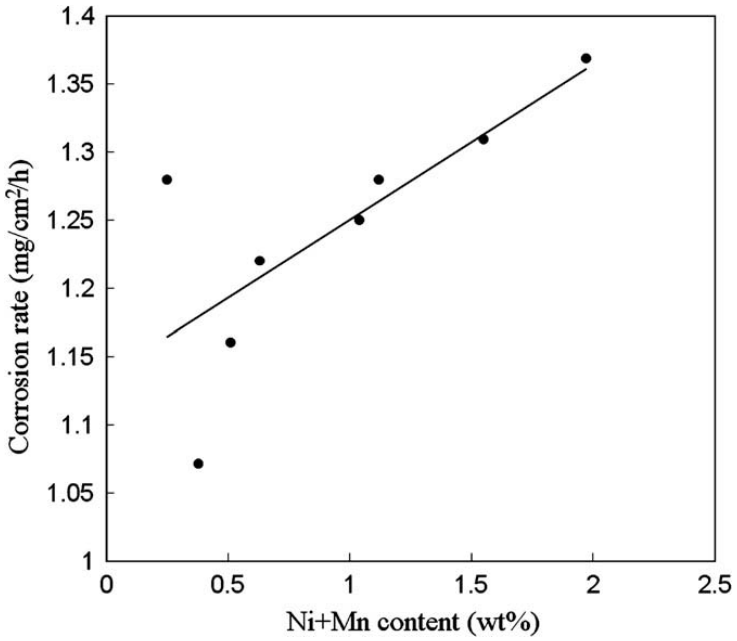

Figure 2.2.1: Rate of nickel corrosion as a function of nickel content reproduced from Zhang [37]

Where R is the universal gas constant, T is the temperature, and a is the activity of the different species present, the metal oxide, metal, and oxygen. Since the metal oxide and metal are solid species, the activity of these is unity, and the activity of oxygen, assuming it is present in the gas phase, can be approximated as the partial pressure of oxygen. Therefore, equation 2.2 can be rewritten to give the partial pressure of oxygen required for certain metal oxide formation by the following equation:

$$p_{O_2} = exp(\frac{\Delta_f G^{\circ}_{M_xO_y}}{RT}) \tag{2.3}$$

Using these equations an Ellingham diagram can be constructed to depict the thermodynamic stability of certain metal oxide species at a variety of temperatures and oxygen partial pressures figure 2.2.2 [40].

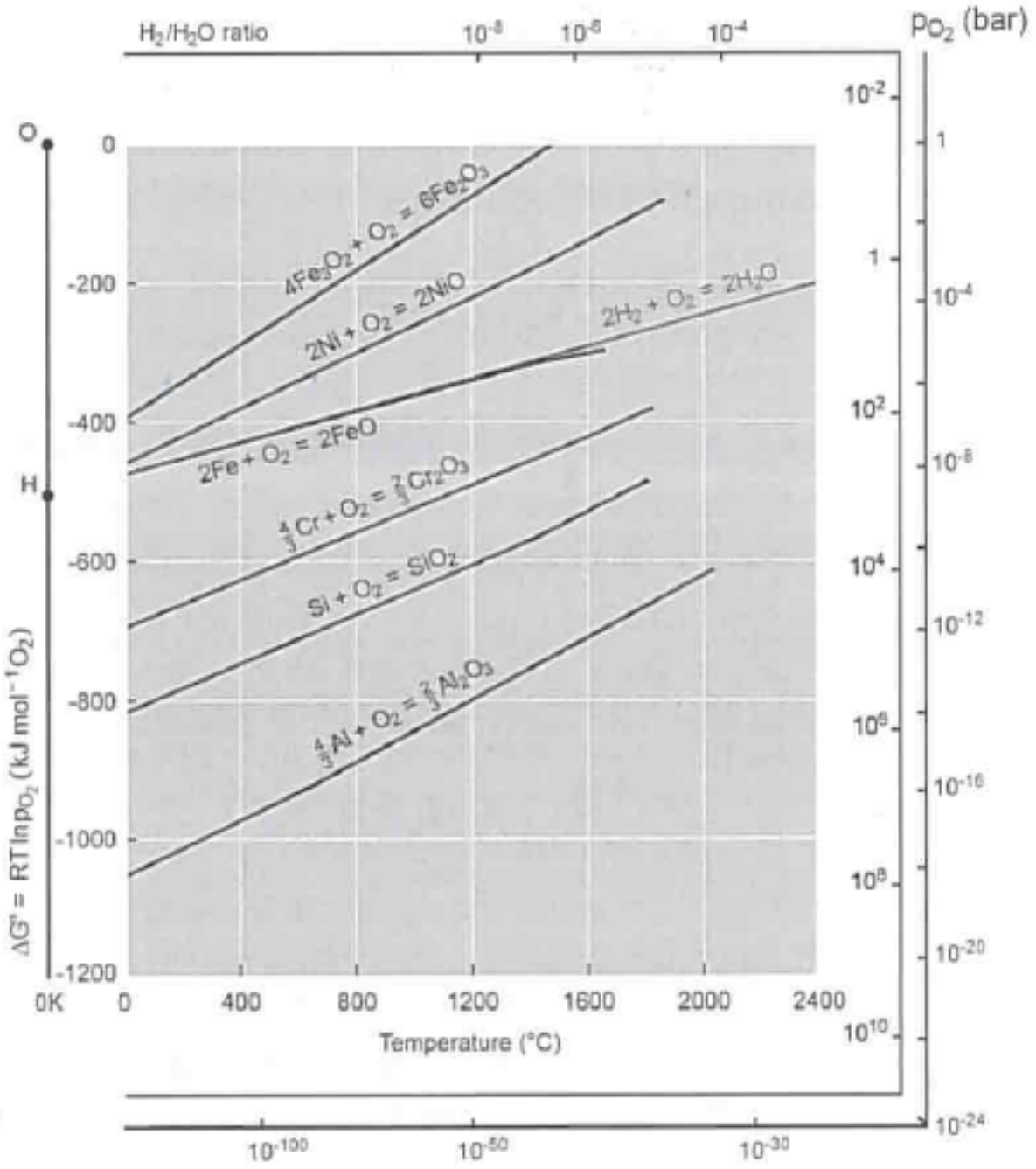

Figure 2.2.2: Ellingham diagram displaying the thermodynamic stability of metal oxides

If the conditions are favorable for the formation of an oxide scale, the oxide scale formation occurs by adsorption of oxygen onto the metal surface. Nucleation of metal oxide at favorable sites on the surface leads to grain growth until the entire surface is covered in a thin oxide film. The film can then continue growing in width by by oxidizing the metal beneath the oxide surface and being added to the oxide film from the bottom as oxygen is reduced at the surface and is added to the top of the film. Stresses that will be applied to the metal, and in turn the oxide, throughout its lifetime will cause defects and, in some cases, cracks in the oxide film. A similar process where further oxidation of the metal and reduction of oxygen gas allows for the self-healing of oxide films [41]. This process is depicted in figure 2.2.3 adapted from Kofstad [42].

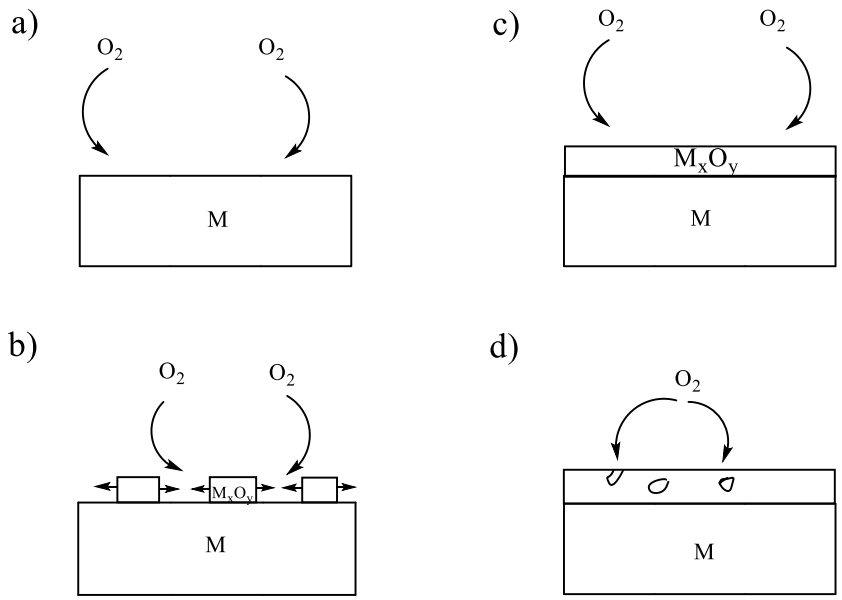

Figure 2.2.3: Oxide scale formation on metal, a) adsorption of oxygen, b) nucleation and grain growth, c) oxide film growth, d) self-healing of defects and cracks

2.2.2 Oxygen Control in Liquid Lead Environment

The oxygen concentration needs to be controlled for the oxide scale formation on the surface of the steel does not occur if the oxygen concentration is too low. However, if the oxygen concentration is too high lead oxide will start to precipitate risking congesting the whole system. In the Ellingham diagram in figure 2.2.4, the red circle highlights this operating region. In practical applications, the partial pressure of oxygen is controlled by controlling the H_2 to H_2O ratio of the gas above the lead [43]. The relationship between the H_2 to H_2O ratio and the oxygen partial pressure above the lead melt is given by the following equation:

$$p_{O_2} = \frac{p_{H_2O}^2}{p_{H_2}^2} exp(\frac{2\Delta_f G^\circ_{H_2O}}{RT}) \tag{2.4}$$

In order to relate the partial pressure to the activity of oxygen in the liquid lead, which will ultimately be responsible for the oxidation of the steel components, the oxygen activity coefficient (γ_0) needs to be known, which can be calculated from the following expressions:

$$a_O = \gamma_0 * c_O = \frac{c_O}{c_O, s} \tag{2.5}$$

where a_0 is the activity of oxygen, c_O is the concentration of oxygen, and c_O the concentration of oxygen in the saturated solution. When the system reaches equilibrium, the solubility of oxygen will be equal to the square root of the partial pressure of oxygen above the lead, as given by the following equation:

$$\frac{c_O}{c_O, s} = \sqrt{\frac{p_{O_2}}{p_{O_{2,s}}}} \tag{2.6}$$

Combining equations 2.4 and 2.6, a relationship between the concentration of oxygen in the lead and the partial pressure of oxygen above the lead can be established:

$$\frac{c_O}{c_{O,s}} = \frac{p_{H_2O}}{p_{H_2} * \sqrt{p_{O_2,s}}} exp(\frac{2\Delta_f G^\circ_{H_2O}}{RT}) \tag{2.7}$$

At this point, a correlation between the saturated oxygen concentration is needed. Correlations such as these have been well documented throughout the literature, with a large number of experiments being summarized in the OECD-NEA Lead Handbook [17]. The following correlation has good agreement with experimental values in the

temperature range of 300 - 1100 °C:

$$logc_{O,s} = 3.32 - \frac{5043}{T} \tag{2.8}$$

With a final combination of equations 2.7 and 2.8 the dissolved oxygen concentration in the lead can be calculated. The results are included in the Ellingham diagram as dashed lines indicating the constant oxygen concentration in the lead 2.2.4.

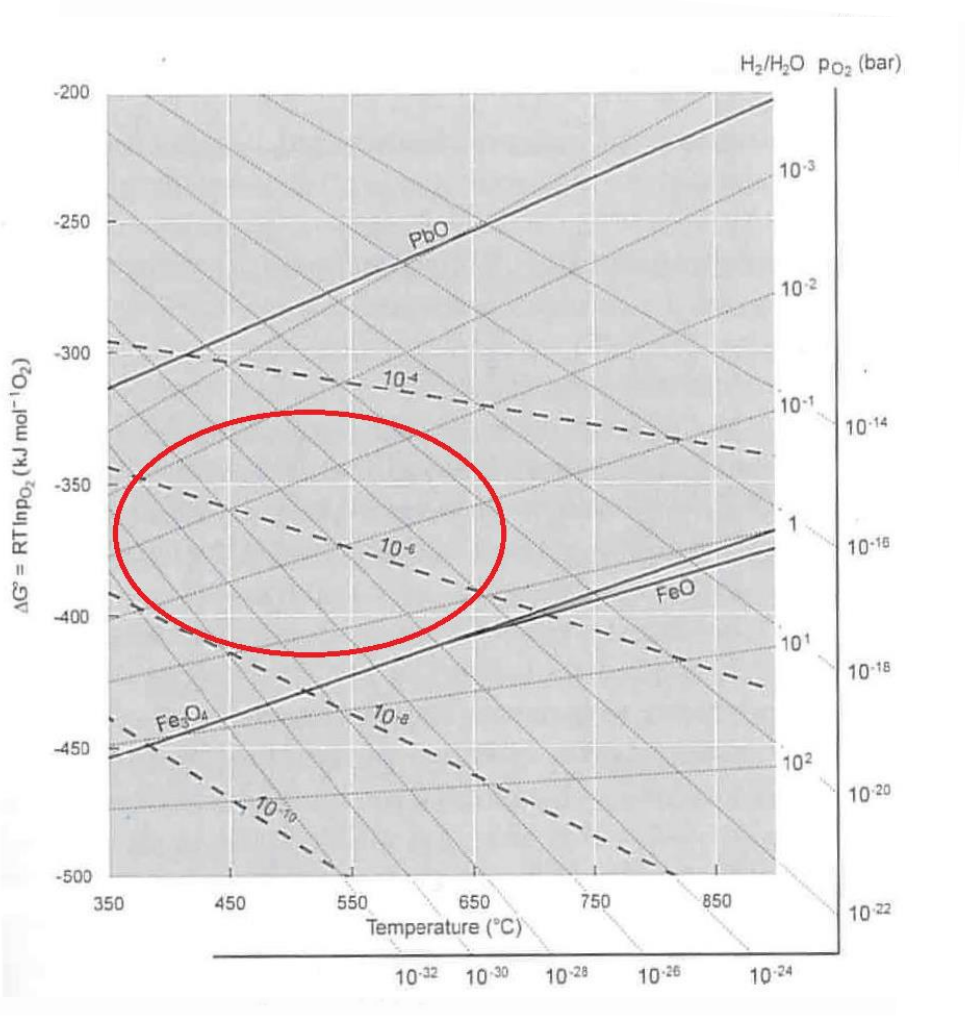

Figure 2.2.4: Ellingham Diagram depicting a magnified view of the intended operating area for lead based systems including oxygen concentrations as dashed lines

2.3 Liquid Metal Embitterment

LME is a non-chemical form of material performance degradation which sometimes falls under the corrosion umbrella. LME is when an ordinarily ductile metal becomes embrittled in contact with a liquid metal counterpart. This loss in ductility leads to a reduction of elongation, in a SSRT set-up, with intergranular and transgranular brittle breaking modes[17]. LME occurs by the nucleation of a crack at the wetted surface of the solid metal and the propagation through the bulk of the metal. There are some requirements for LME to occur:

- Intimate contact between liquid metal and solid metal. In a classical concept, this is good wetting of the solid metal
- LME must be preceded by plastic deformation

- There should be some obstacles to dislocation motion, which will cause stress concentrators triggering a brittle break

The LME phenomenon usually has a very limited temperature range just above the melting temperature of the liquid metal. At higher temperatures, the solid metal recovers all ductility. For T91 steel in LBE, the temperature range in which it is embrittled is 160-350°C, while in lead, this temperature range is 340-400°C [44].

Given that LME requires an intimate contact of the solid and liquid metals, the protective oxide layer will act as an inhibitor to the wettability of the solid metal. LME is promoted by limited solubility of the metals with one another, whereas solid-liquid couples that tend to form intermetallic compounds tend to inhibit LME. This trend has been documented and reported by Cramer et al. depicted in Figure 2.3.1 [45].

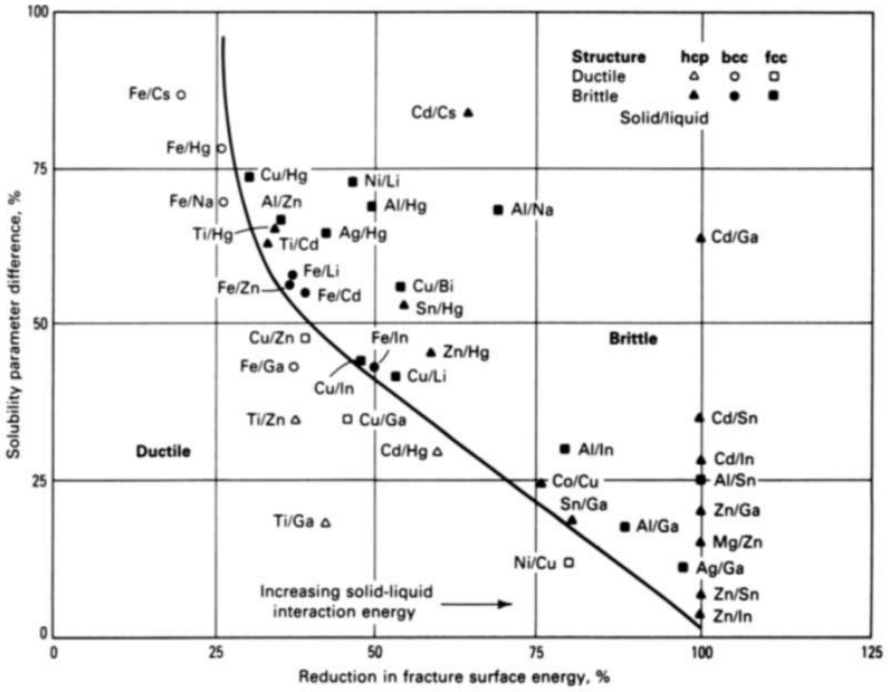

Figure 2.3.1: Reduction in the fracture surface energy relating to solubility parameter for different solid-liquid couples with a curve separating the ductile and brittle fracture modes

For the solid itself, the microscopic structure is very relevant to the potential propagation or prevention of the LME phenomenon. The main characteristic that should be noted is the grain size which shows a trend of increasing grain size increases

the LME effect [44]. This is due to the diffusion rates along grain boundaries being faster than through the bulk of the metal. This means that stress concentrators will not build up as rapidly as there is less of an obstacle to dislocation motion. While this is a general correlation, this is not a rule, and there are examples, for instance a high entropy alloy with an FCC unit cell being very resistant to LME despite having grains as large as 1mm [46]. FCC crystal structures, i.e., austenitic steel, tend to be less susceptible to LME than the BCC crystal structure, i.e., ferritic steel, counterparts. Furthermore, the solid metal is only embrittled while in contact with the liquid metal. This means there is no permanent change to the solid metal's mechanical properties assuming no critical crack propagation has started [47].

While the topic of LME is still not fully understood mechanistically, there are a few models which will be presented here. It should be noted that these models are based on experimental observation using pure element liquid-solid couples and are based on single crystals solid metals. This makes the models not very transferable between different set-ups and especially not when it comes to predicting the potential solid-liquid metal couples which may be susceptible to LME.

2.3.1 Models

Reduction in Surface Energy Model

The reduction in surface energy model is one of the most widely accepted explanations for the mechanism of LME. It is based on the classical Griffith approach for brittle fracture while taking into account the Rebinder effect proposed in the first study on LME [48]. The Rebinder effect is the reduction in the hardness and ductility of a material decreases due to a film of active surface molecules. The fracture occurs when the energy in the system is stored as elastic energy in the crack tip, and the work required to move the external surfaces becomes greater than the energy required to form a new surface. The elastic energy released by the crack tip, which should be equal to the surface energy (γ_e), is given by $\frac{K^2}{E}$, where K is the stress intensity factor. The stress intensity factor is given by the following expression, $K = \sigma * \sqrt{a}$. Combining the previous two expressions gives an expression for the critical stress value for a crack of given length (a) [44]:

$$\sigma_c = \sqrt{\frac{E * \gamma_e}{a}} \tag{2.9}$$

where σ_c is the critical stress value, E is the Young's modulus, γ_e is the specific surface energy and a is the length of the crack. The surface is reduced by the solid-liquid interaction in a LME case ($\gamma_{LME} < \gamma_e$). While the model is very simplistic in principle, only requiring the reduction in surface energy, it is rarely used to quantitatively define a LME couple as the surface energy is not easily measurable. It is well known that the displaced energy from plastic deformation is significantly larger than that of the surface energy. This leads to the fundamental issue of this model: it only considers the elastic deformation and not the crack plasticity. This can be accounted for by using the effective surface energy as a sum of the plastic displacement energy and surface energy:

$$\gamma_f = \gamma_p + \gamma_e \tag{2.10}$$

Since $\gamma_p > \gamma_e$ during LME, the plastic displacement energy must be reduced. However, in a macroscopic stress-strain curve, the difference between the ductile and brittle breaks is not significant suggesting that the plastic growth mechanism is in fact changing.

Another shortcoming of the reduction in surface energy model is that metallurgical and physical variables are not accounted for in a clear manner in their effect on the LME phenomenon, nor does it provide any mechanistic insight at the atomic scale.

Adsorption-Induced Reduction in Cohesion Model

The adsorption-induced reduction in cohesion model can be seen as an extension of the previous reduction in surface energy model by including a potential atomic mechanism in the explanation. The growth rate of the crack is typically very fast. Therefore, the diffusion of metal atoms in the solid out to the liquid would be too slow to account for the LME effect. Alternatively, this model proposes that the embrittling effect is caused by the adsorption of the liquid metal atom at the crack tip in the solid as depicted in figure 2.3.2 [49].

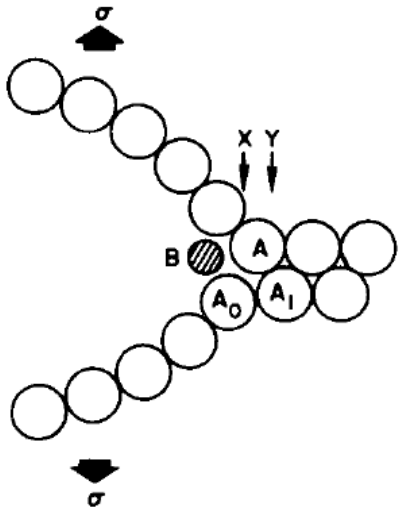

Figure 2.3.2: Illustration of the adsorption of liquid metal atom (b) on the crack tip of solid metal (A)

The adsorbed liquid metal atom only affects the very small volume at the crack tip, which means that this model assumes that the adsorbed liquid metal reduces the intermetallic bond strength of the solid metal. After accounting for this equation 2.9 becomes:

$$\sigma_c = \sqrt{\frac{E\gamma_{e_{(B)}}\rho/a_0}{4a}} \tag{2.11}$$

where $\gamma_{e_{(B)}}$ is the intermetallic bond strength between the liquid and solid metals, ρ is the crack tip radius and a_0 is the critical crack radius. This incorporation of the intermetallic bond strength is supported by the solubility effect. Two metals with high mutual solubility are less likely to undergo LME since samples with a high solubility tend to form intermetallic compounds with larger intermetallic bond strengths.

Under this model, a constant supply of the liquid metal atoms are required at the crack tip. Therefore the rate of embrittlement is limited by the transport rate of the liquid metal. While the model has been used with some success, it does require a good estimate of the cohesion strength, which is measurable or approximated using first principles. The prediction of the crack growth is still limited in this model as it requires information on the underlying chemistry, namely the diffusion of the liquid metal to the crack site and the adsorption of the liquid metal onto the solid. These two effects are both related to temperature. As the temperature increases, the diffusion

rate of the liquid also increases. In turn, the adsorption rate, or time that a, atom is adsorbed on the metal surface decreases, which is an explanation for the recovery of ductility at higher temperatures. This model does propose an atomic-scale mechanism for embrittlement. However, it does not address the microstructure of the solid metal. For instance if adsorption is more favorable at sites with large strain, adsorption would be promoted at grain boundaries or other stress concentrator sites. These factors make the predictions with this model difficult to nearly meaningless in many cases [44].

Enhanced Dislocation Emission Model

The enhanced dislocation emission model is also based on the liquid metal's adsorption onto the solid. Rather than reducing the intermetallic bond strength, this model proposes a reduction in the shear strength of the metal [50, 51]. The proposed mechanism is an adsorption-induced dislocation emission and micro-void coalescence. This occurs by the reducing the shear strength induced by the adsorbed liquid atom, which results in the injection of dislocations on suitably inclined slip planes at the crack tip. The strain needed to link up the crack with nano-sized voids ahead of the crack tip is much smaller compared to normal ductile tearing, this mechanism is depicted in figure 2.3.3.

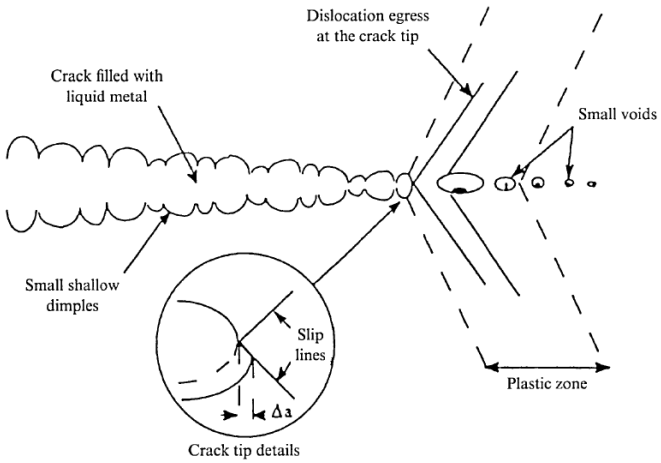

Figure 2.3.3: Schematic of the crack growth by micro-void coalescence proposed by the enhanced dislocation emission model

The nano-voids are at a size where only high magnification levels in scanning electron microscopy (SEM) or transmission electron microscopy (TEM) images can determine

them. The fracture mode on the surface, usually cleavage fracture mode, can be hard to see in lower resolution. Distinguishing the micro-plasticity and the cleavage may therefore be difficult, leading to the most common criticism of this model being that it may be an artifact. In other words it is a fabrication of the testing conditions. Furthermore, the model is purely mechanistic, which makes the applicability of quantitative predictions nonexistent.

2.3.2 Steel-Lead/LBE Couple

It has been demonstrated that austenitic steels with an FCC unit cell are less susceptible to LME than the ferritic steels with a BCC unit cell counterpart [52]. However, austenitic steels do have the dissolution issue, which means ferritic steels such as T91 or the alumina forming ferritic FeCrAl are currently primary candidates for components in an LFR. These metals have demonstrated susceptibility to LME in liquid lead and LBE melt [53–57]. It was also demonstrated that LME was only an issue at a low-temperature range just above the melting point. Temperature dependant studies have been conducted with various ferritic steel and LBE couples which determined that a ductility recovery occurred around 450$^{\circ}C$ after the most strongly embrittling condition of around 350-375$^{\circ}C$ [55, 57]. The strain rate also had a significant contribution on the LME phenomenon, with low strain rates having a significantly higher embrittlement effect than faster strain rates suggesting there that LME has a slow embrittlement rate [52, 54]. In terms of liquid metal and ferritic steel, a couple of investigations have shown that LBE has a stronger embrittling effect than pure bismuth, which has a more substantial effect than pure lead [54]. This is troubling for reactors that intend to utilize the low melting point of LBE, such as the MYRRHA reactor, MicroURANUS, or the SVBR [58].

Commercial FeCrAl alloys have also been investigated, suggesting that LBE strongly embrittles these alloys with the temperature-dependent reduction in ductility from 150-450$^{\circ}C$ [53, 56, 57]. The alumina layer does have a protective effect to corrosion but more importantly, on LME as well. Tests were conducted in both oxygen-depleted and oxygen saturated LBE which showed a signficant reduction in the total elongation of the sample in an oxygen-depleted environment [53]. The composition of the FeCrAl affects the material's susceptibility to LME. Three FeCrAl alloys were tested with chromium and aluminum content of 10-4, 15-4, and 10-6 respectively. It was found that from most to least embrittled were the 10-6, 15-4, and 10-4 alloys. It was seen

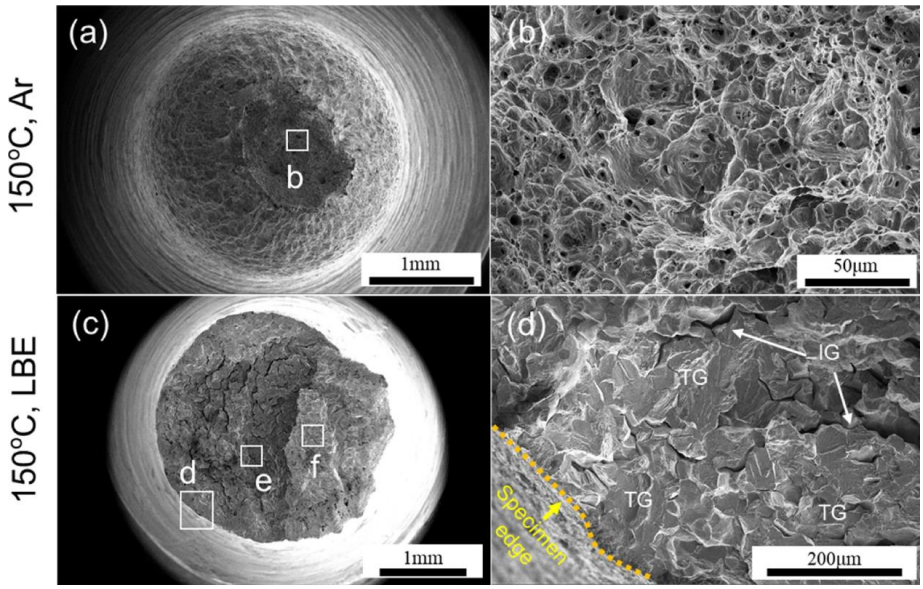

Figure 2.3.4: a) and b) ductile break of sample drawn in Argon at 150°C c) and d) brittle break of sample drawn in LBE at 150°C reproduced from [57]

that the 10-6 had the largest grain size and the 10-4 had the smallest, suggesting that the grain size does indeed influence on the LME phenomenon, as mentioned in section 2.3 [56].

The macroscopic engineering stress-strain curve can be used to see a reduction of elongation, which demonstrates a reduction in ductility. The SEM can confirm the macroscopic observation of the stress-strain curve on a microscopic level. In figure 2.3.4 the difference between the ductile breaking mode and the brittle breaking mode can be observed. The ductile break has the characteristic dimple formation, while the brittle break of the sample in LBE is transgranular cleavage with numerous intergranular cracks, which are much more defined and are characteristic of a brittle fracture.

Chapter 3

Set-up and Methodology

3.1 SSRT Rig

The set-up used of the SSRT rig, which was developed at KTH to study the LME phenomenon, is shown in figure 3.1.1. The SSRT main components are the precision linear actuator, load cell, gas-tight vessel, drawbars, the crucible, and U-shaped bracket. All components in contact with the liquid lead or LBE – such as the detachable drawbar, the crucible and the U-shaped bracket – are all made of the 10-4 FeCrAl to prevent corrosion of the internal components and extend the lifetime of the SSRT rig. The actuator was purchased from Thomson and is the PC40 model, with a maximum load of 5000 N and a stroke length of 1200 mm with an error of $\pm$ 0.001mm [59]. It is an electric design rather than a traditional hydraulic which means it is more compact and easier to service when required. The actuator is also more accurate, allowing for complete control of the velocity, position, torque, and force applied on the sample.
The gas-tight expansion joint allows for movement of the drawbar to apply a strain on the sample while maintaining an oxygen-free environment. The joint is attached to the vessel's lid via two 316L plates with a copper seal to ensure that it is gas-tight.The drawbar is divided into two parts. The top part that connects to the actuator is made of 316L steel and the lower detachable part which is made of 10-4 FeCrAl as it is in contact with the liquid metal environment throughout the test. The lower drawbar also has threads that allow the sample to fasten into it. Below this, the U-shaped bracket, also made of 10-4 FeCrAl, holds the other end of the sample by a removable bolt with threads. The inner crucible that holds the stagnant liquid metal is made of 10-4 FeCrAl and is removable so that the testing environment can be changed.

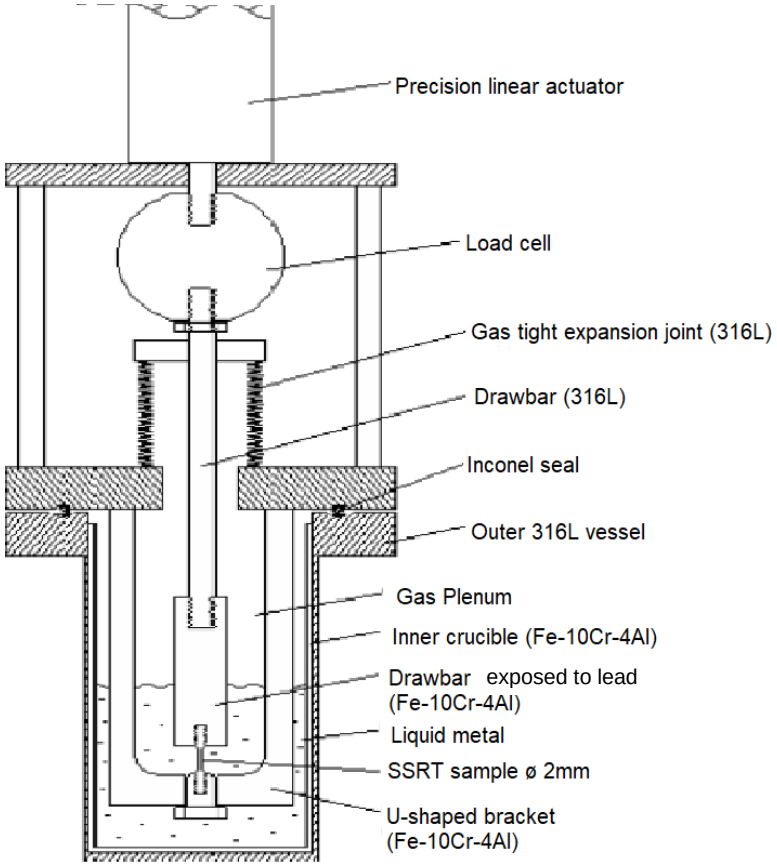

Figure 3.1.1: The SSRT rig schematic

3.2 Test Parameters

3.2.1 LME Dependency on Temperature

The two liquid metal environments for this series of tests were pure lead and LBE, with a composition of 58.5 wt% bismuth and 41.5 wt% lead. The FeCrAl sample was wetted at 450$^{\circ}C$ in the stagnent liquid metal environment for 24 hours to ensure intimate contact between the liquid and solid metals. The temperature was then reduced to the testing temperature between the melting point and 450$^{\circ}C$. For LBE, this range started at 140$^{\circ}C$ and for lead, this range started at 340$^{\circ}C$. An Ar/5% H_2 gas flowed at a speed of 80 ml/min over the lead environment ensuring a low oxygen environment inside the rig. The oxygen concentration in the gas above the lead is measured using yttria-stabilized zirconia (YSZ) oxygen probe (Zirox SGM5 sensor) [60]. The sensor confirmed that the oxygen partial pressure was around 10-11 wt% O before the experiment began and throughout the whole test, limiting the effect of the oxide formation on the steel surface. Once the test begins, the strain rate is set to 10^{-5} s^{-1} or 10^{-6} s^{-1}. As already seen in previous work, a slower strain rate resulted in a more significant embrittling effect. Therefore to confirm if samples at a certain temperature were truly ductile, a slower strain rate was used. The FeCrAl samples were all made to fit the specification shown in figure 3.2.1 and were received from Kanthal hot worked and annealed according to their set standards. A reference for the ductility of the natural sample was drawn at room temperature in a non-liquid metal environment.

3.2.2 LME Dependency on Bismuth Concentration

After completion of the lead temperature series, the bismuth wt% was slowly increased by adding LBE. The SSRT was repeated according to the same parameters above. First, the sample was left in the oxygen-depleted liquid metal environment at 450$^{\circ}C$ for 24 hours before reducing the temperature to the test temperature of 375$^{\circ}C$. 375$^{\circ}C$ was selected as it was seen that at this temperature the liquid metal had the largest reduction in ductility, as will be demonstrated later. The test strain rate was set to 10^{-5} s^{-1} and occasionally the test was repeated at 10^{-6} s^{-1} again to confirm the ductility of a sample. The FeCrAl samples were prepared as the previous group to fit the specifications shown are in figure 3.2.1.

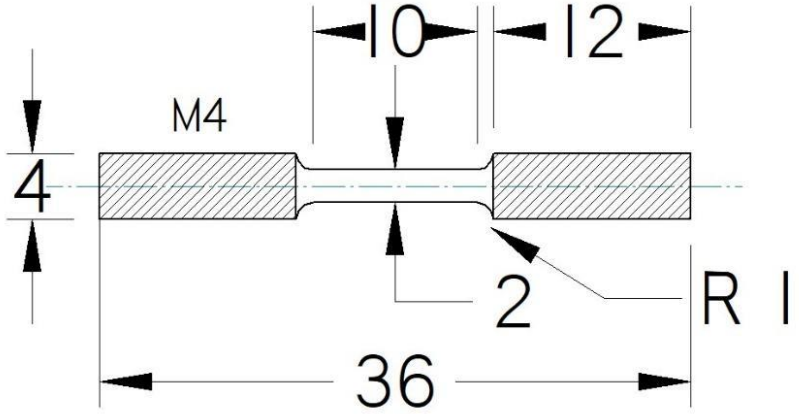

Figure 3.2.1: FeCrAl SSRT sample specifications in mm

3.2.3 Sample Analysis

After the experiment, the samples were cleaned using a mixture of acetic acid ($C_2H_4O_2$), hydrogen peroxide (H_2O_2), and deionized water. If the sample was broken in the LBE environment, the ratio of the solution was 1:1:1, respectively. If the sample was broken in the Pb environment, the ratio of the solution was 1:1:7. The samples were submerged in the solution for 45 min to 1h, or until the bubbling had stopped. They were rinsed off using water and dried.

The samples were then characterized and analyzed using a Philips XL 30 SEM, with an energy dispersion spectroscopy (EDS) analyzer allowing for elemental analysis.

Chapter 4

Results

4.1 Reference

An initial sample was drawn in the absence of a liquid metal to be used as a control result for a ductile sample. The conditions of the test in terms of strain rate and temperature, as well as the characteristics of the metal in terms of the yield strength (YS), ultimate tensile strength (UTS), and the elongation to failure are presented in table 4.1.1.

Table 4.1.1: Test conditions showing the temperature, nominal strain rate, yield strength, ultimate tensile strength (UTS), and elongation to failure in an air environment

Temperature[°C]	Nominal Strain Rate [s^{-1}]	Yield strength (σ0.2) [MPa]	UTS [MPa]	Total elongation to failure [%]
25	$3*10^{-6}$	440	547	20

From the SSRT data, an engineering stress-strain curve is constructed, which is presented in figure 4.1.1. In the figure, there are three points of interest. The first point of interest is point A, which is the YS, when the elastic deformation zone ends and the plastic deformation begins. Point B is the UTS, after which point the necking formation begins. Finally, point C is the point of the of the sample breaking. In a ductile sample, such as the reference sample conducted in air, the amount of strain between the UTS and the final break is significant, allowing for a cup formation around the breaking point of the sample. Whereas in a brittle sample the strain from the UTS to the breaking point is significantly smaller which means there will be a very small neck

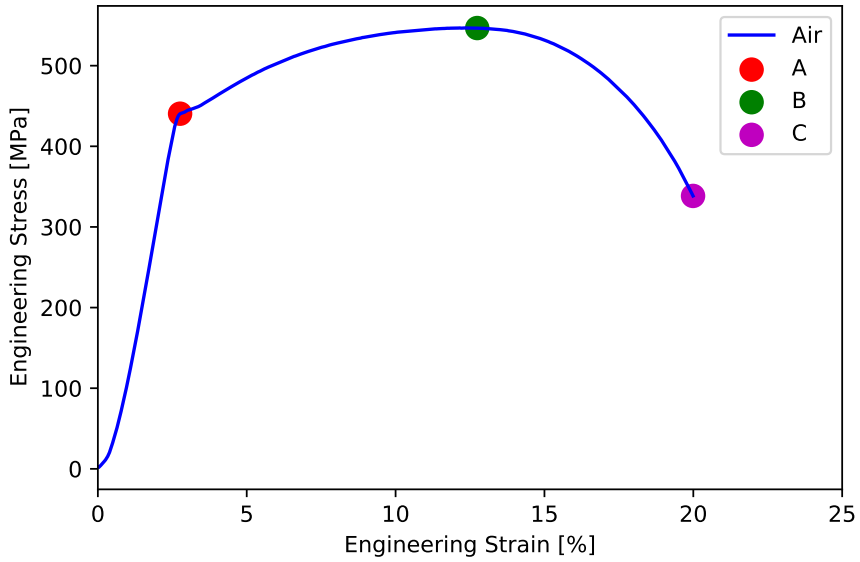

Figure 4.1.1: Engineering stress-strain curve for the SSRT in air at room temperature

formation.

4.2 Temperature Dependency in Lead

The conditions of the tests conducted in liquid lead in terms of strain rate and temperature, as well as the characteristics of the steel in terms of the YS, UTS, and the elongation to failure are presented in table 4.2.1.

Table 4.2.1: Test conditions showing the temperature, nominal strain rate, yield strength, ultimate tensile strength (UTS), and elongation to failure in a lead environment

Temperature[°C]	Nominal Strain Rate [s^{-1}]	Yield strength ($\sigma_{0.2}$) [MPa]	UTS [MPa]	Total elongation to failure [%]
340	$6.36*10^{-6}$	400	540	25.0
350	$5.81*10^{-5}$	398	517	25.5
360	$3.53*10^{-5}$	390	534	25.0
370	$4.00*10^{-5}$	388	532	25.0
375	$7.23*10^{-5}$	351	473	24.7
380	$3.64*10^{-5}$	379	518	24.8
390	$3.41*10^{-6}$	352	501	25.0
400	$6.42*10^{-5}$	368	485	22.5
420	$3.50*10^{-6}$	367	488	25.9
450	$3.55*10^{-6}$	366	476	24.2
480	$4.44*10^{-6}$	350	455	25.0

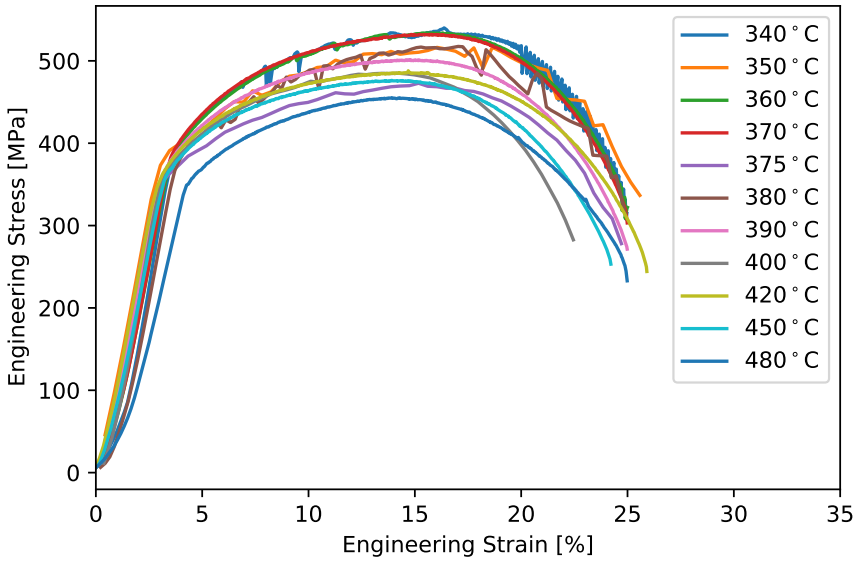

Figure 4.2.1: Engineering stress-strain curve for the SSRT in liquid lead across the temperature series

From the SSRT data, an engineering stress-strain curve is constructed, which is presented in figure 4.2.1. The YS and UTS are unaffected by the different temperatures occurring at the same strain percentage, around 3% and 11%, respectively. The reduction in the stress at the YS and UTS as the temperature increases is a result of the metal becoming softer, i.e., losing strength at higher temperatures. The total elongation to failure for all temperatures is greater than 20%, around 25%. These total elongation to failure values are comparable to the reference value of 20% presented by the sample in the inert environment suggesting that these sample breaks are normally ductile. The samples have an increased amount of elongation up to 6% over the reference sample due to the increased temperature softening the steel. These values indicate no effect of LME in a pure lead environment.

The SEM images of the samples broken in pure lead at 350°C and 375°C are given in figure 4.2.2. The samples had a very strong neck formation as depicted in figure 4.2.2 A, C, which indicates a large amount of strain after the UTS. Additionally, the fracture surface has a strongly dimpled surface characteristic of a ductile break. As the sample is drawn in the necking phase of the break microvoids are formed in the material which are left as evidence in the depression on the surface of the materials known as dimples as seen in figure 4.2.2 B, D. Further providing evidence that these samples are ductile in pure lead and are not susceptible to LME in these environments.

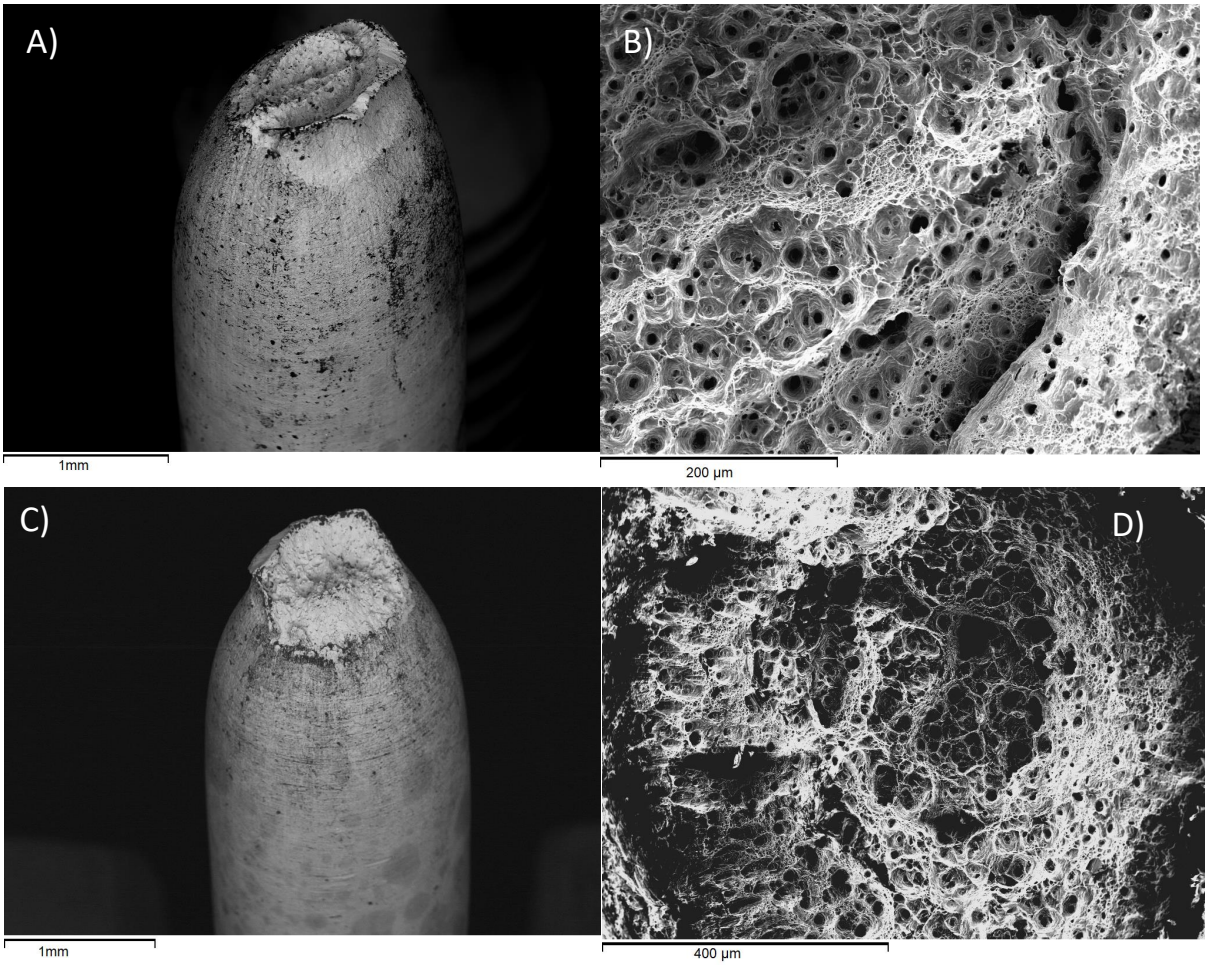

Figure 4.2.2: SEM images of fracture surfaces of various samples from pure lead A) side view of 350°C, B) surface view of 350°C, C) side view of 375°C, D) surface view of 375°C

4.3 Temperature Dependency in LBE

The conditions of the tests conducted in liquid LBE in terms of strain rate and temperature, as well as the characteristics of the steel in terms of the YS, UTS, and the elongation to failure are presented in table 4.3.1.

From the SSRT data an engineering stress-strain curve is constructed, which is presented in figure 4.3.1. The YS and the UTS are unaffected by the different temperatures occurring at the same strain percentage, around 3% and 13%, respectively. As seen with the samples in the lead, there is a reduction in the stress at the YS and UTS as the temperature increases, which is again a result of the steel becoming softer at elevated temperatures. The total elongation to failure reduces from around 20% at temperatures of 140-250°C down to 13% elongation at 375°C at its

Table 4.3.1: Test conditions showing the temperature, nominal strain rate, yield strength, ultimate tensile strength (UTS), and elongation to failure in a LBE environment

Temperature[°C]	Nominal Strain Rate [s^{-1}]	Yield strength ($\sigma 0.2$) [MPa]	UTS [MPa]	Total elongation to failure [%]
140	$6.60*10^{-5}$	424	516	22.6
170	$5.88*10^{-5}$	407	519	22.2
195	$5.77*10^{-5}$	404	519	18.7
250	$5.31*10^{-5}$	389	524	19.1
300	$6.13*10^{-5}$	396	534	16.6
325	$5.36*10^{-5}$	374	498	16.4
350	$5.57*10^{-5}$	369	496	15.7
375	$5.33*10^{-5}$	377	505	13.1
400	$6.50*10^{-5}$	377	505	18.3
425	$5.60*10^{-5}$	379	477	20.5
450	$7.31*10^{-5}$	383	461	25.9

worst. This indicates that there is an LME effect in the LBE environment. This is then followed by a recovery of ductility starting at at 375°C when the total elongation to failure begins to increase until complete recovery of ductility at 450°C. The YS and the UTS were unaffected by the LME phenomenon.

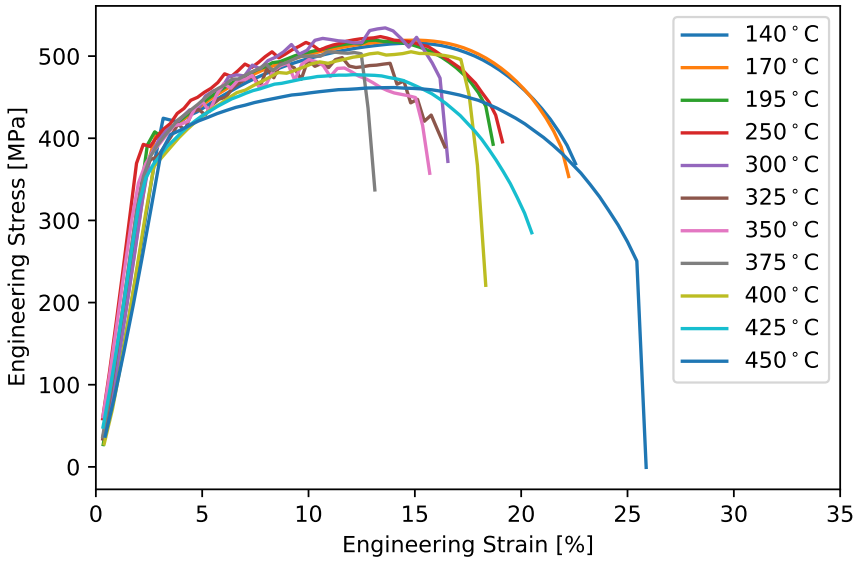

Figure 4.3.1: Engineering stress-strain curve for the SSRT in liquid LBE across the temperature series

The SEM images of the fracture surface, that verify the results described, are shown in figure 4.3.2. There is a strong necking effect indicating that the sample has undergone large amounts of plastic deformation after the UTS was reached, as seen in figure 4.3.2 A, E. It is commonly accepted that the LME effect only starts after the necking process has begun, i.e., after the UTS has been reached. This notion is supported by the YS and the UTS being unaffected by LME. Therefore, the minimal neck formation on the sample broken at 300°C indicates that the sample is brittle and was broken shortly after the UTS was reached, as seen in figure 4.3.2 C. The surface views showing large dimple formations on the sample also provide more evidence for the ductile breaks of the samples that were broken at 140°C and 425°C in figure 4.3.2 B, F. In the sample broken at 350°C, there is an entirely different picture here cleavage in the form of intergranular cracks and transgranular cracks are the common fracture modes as indicated by the jagged nature of the fracture surface seen in figure 4.3.2 D. The brittle features of both the crack surface and side view indicate that the samples are affected by LME. The sample broken at 195°C shows both brittle and ductile characteristics in the breaking modes, as seen in figure 4.3.3, suggesting that there is a transition point from ductile to brittle fractures. The side view of the FeCrAl sample shows a minor necking effect, less than that of the 140°C sample and that of the 425°C sample, as seen in figure 4.3.3 C. The fracture surface also indicates that the sample has both brittle and ductile characteristics, with figure 4.3.3 A showing the brittle cracking modes on one part of

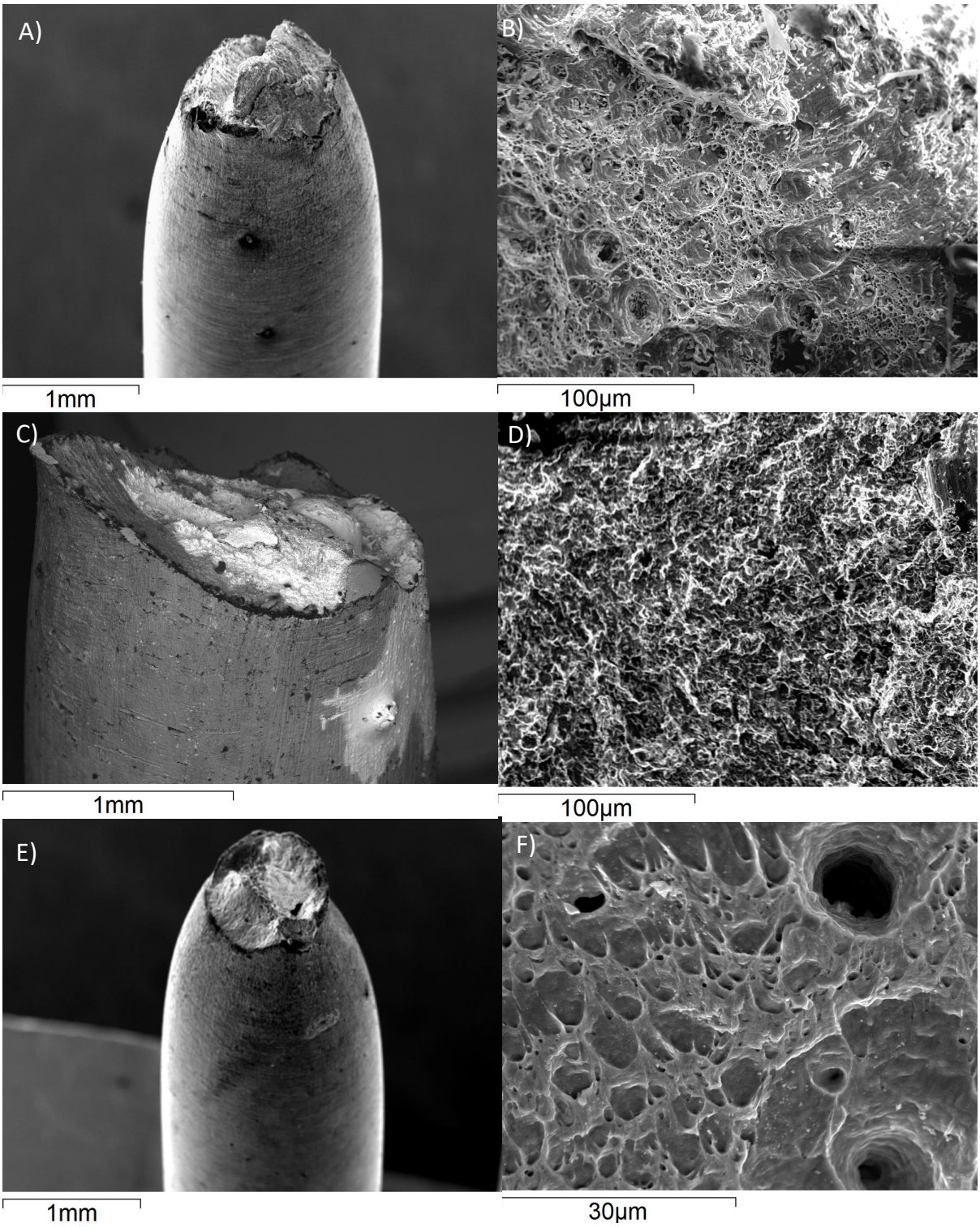

Figure 4.3.2: SEM images of fracture surfaces of various samples from LBE A) side view of 140°C, B) surface view of 140°C, C) side view of 300°C, D) surface view of 350°C, E) side view of 425°C, F) surface view of 425°C

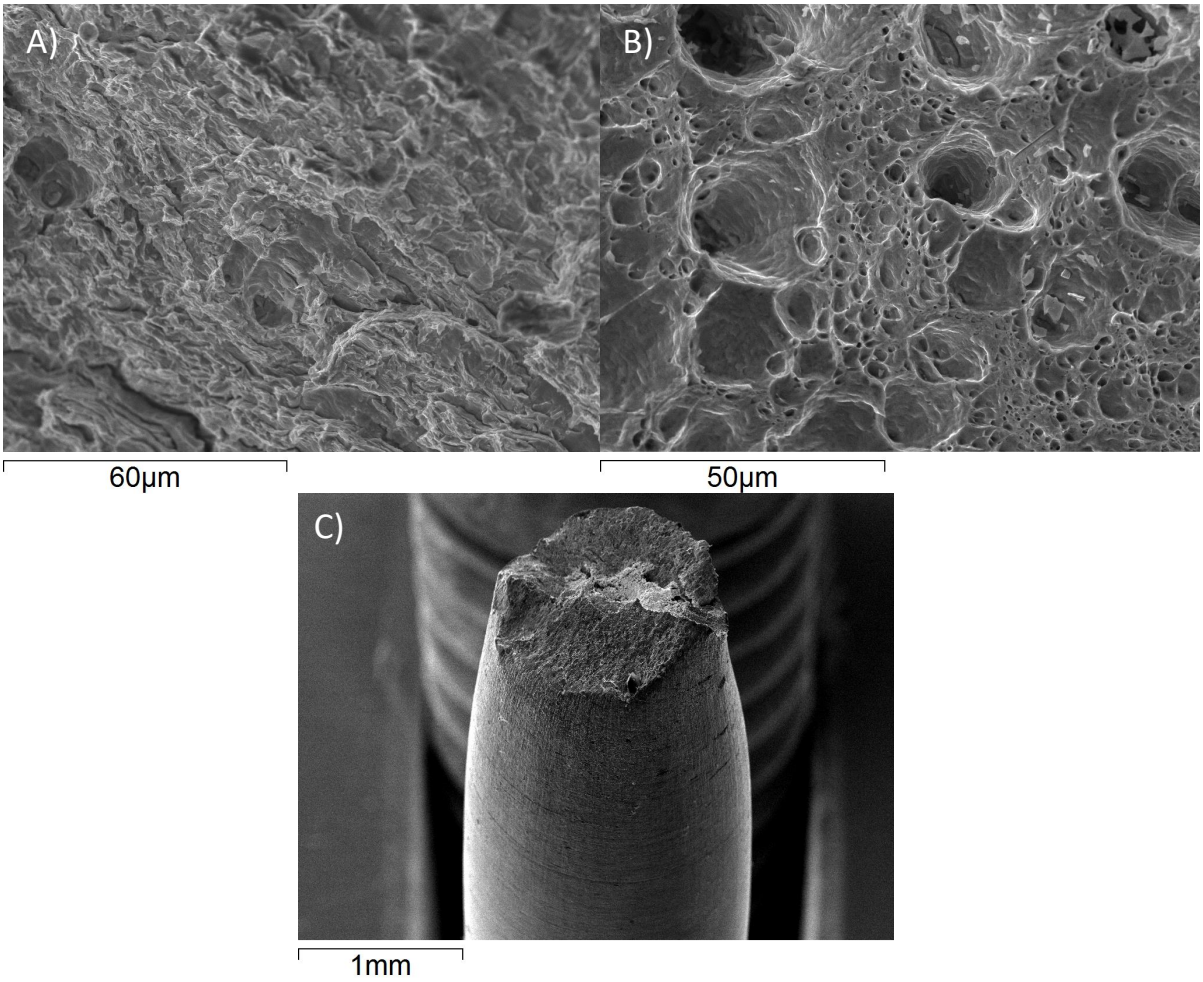

Figure 4.3.3: SEM images of sample broken at 195°C A) brittle fracture mode on fracture surface, B) ductile fracture mode on fracture surface, C) side view

the surface and figure 4.3.3 B showing the ductile dimpled fracture mode on another part of the surface. These results indicate that just below a 20% strain until failure there is a transition point where the breaks go from ductile to brittle. For the FeCrAl steel investigated in this work, this transition point is around 200°C and 425°C for the recovery of ductility in LBE.

4.4 Bismuth Concentration Dependency

The conditions of the tests conducted in the liquid lead-bismuth mixture with varying bismuth weight percents in terms of strain rate and bismuth concentration, as well as the characteristics of the steel in terms of the YS, UTS, and the elongation to failure are presented in table 4.4.1.

Table 4.4.1: Test conditions showing the bismuth weight percent, nominal strain rate, yield strength, ultimate tensile strength (UTS), and elongation to failure in a lead bismuth environment

Bismuth amount [wt%]	Nominal Strain Rate [s^{-1}]	Yield strength ($\sigma_{0.2}$) [MPa]	UTS [MPa]	Total elongation to failure [%]
0.1	$6.88*10^{-5}$	381	504	24.8
1.0	$6.49*10^{-5}$	371	500	24.9
2.0	$6.50*10^{-5}$	370	504	24.9
3.0	$6.36*10^{-5}$	381	507	24.8
5.0	$5.96*10^{-5}$	374	505	19.7
6.0	$5.93*10^{-5}$	379	499	20.0
7.0	$6.04*10^{-5}$	373	501	21.4
8.0	$6.63*10^{-5}$	370	498	20.7
9.0	$5.75*10^{-5}$	371	503	19.0
10.0	$6.08*10^{-5}$	369	498	20.8
12.0	$5.75*10^{-5}$	373	496	19.0
13.0	$6.15*10^{-5}$	372	500	20.7
14.0	$5.79*10^{-5}$	365	494	19.1
15.0	$5.81*10^{-5}$	380	502	18.1
17.5	$5.69*10^{-5}$	371	501	16.4
18.5	$6.02*10^{-5}$	379	504	16.3
19.5	$5.08*10^{-5}$	372	503	17.7
22.5	$5.72*10^{-5}$	381	504	16.1
25.0	$5.72*10^{-5}$	390	495	16.1
30.0	$4.85*10^{-5}$	394	499	12.8
40.0	$5.25*10^{-5}$	392	502	14.5

From the SSRT data, an engineering stress-strain curve is constructed, which is presented in figure 4.4.1. All tests were conducted at a temperature of 375°C, which makes it abundantly clear that the YS and the UTS is unaffected by the LME. The YS and UTS still occur at the same strain percentage of around 3% and 13%, respectively. Since the temperature is the same for all these tests, the magnitude of the YS and the UTS is also in a very similar range, unlike the previous tests, which had a reduction in the magnitude of both the YS and UTS as the temperature increased. Initially, the samples have similar elongation values as the lead, with around 25% elongation to

failure. There is a slight reduction in ductility at 5 weight percent bismuth with the total elongation to failure values of around 20%. The samples maintained this level of total elongation until failure until about 15 weight percent bismuth, where there is another reduction in ductility with a large decrease down to 16.4% elongation at 17.5 weight percent bismuth. The samples maintained a total elongation to failure of around 16-17% from 17.5 weight percent to 25 weight percent bismuth. The final significant drop the in the total elongation to failure down to 13% at 30 weight percent bismuth, which is comparable to the the total reduction in the ductility of the sample at 375°C in LBE.

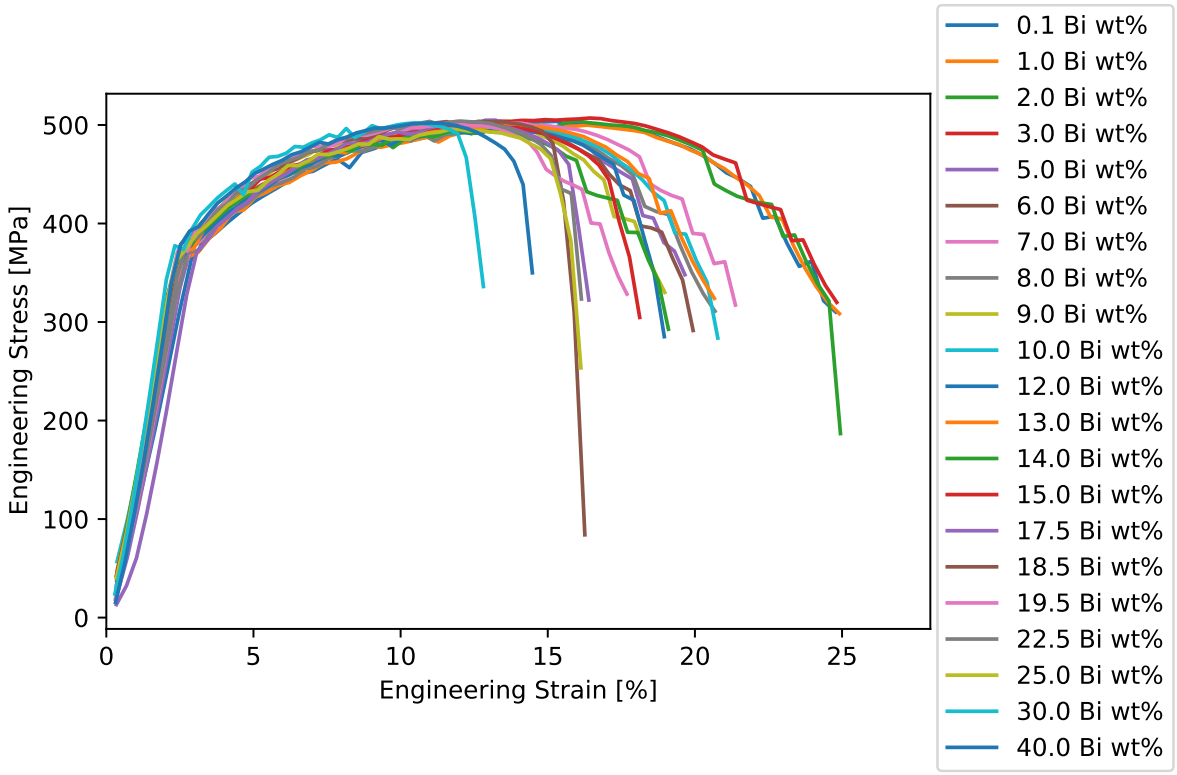

Figure 4.4.1: Engineering stress-strain curve for the SSRT in liquid lead bismuth environment with increasing bismuth weight percent

The SEM images of the sample broken in 1 weight percent are presented in figure 4.4.2. The side view of the sample shown in figure 4.4.2A depicts the strong necking phenomenon that is clearly visible. This suggests that the sample was drawn for a substantial time after the UTS was reached. The surface view of the sample shown in figure 4.4.2B depicts the clear dimple formation of the ductile breaking mode. This provides evidence that the samples that had an elongation of around 25%, i.e., under 5 wt% bismuth in the lead mixture, are ductile in the breaking nature.

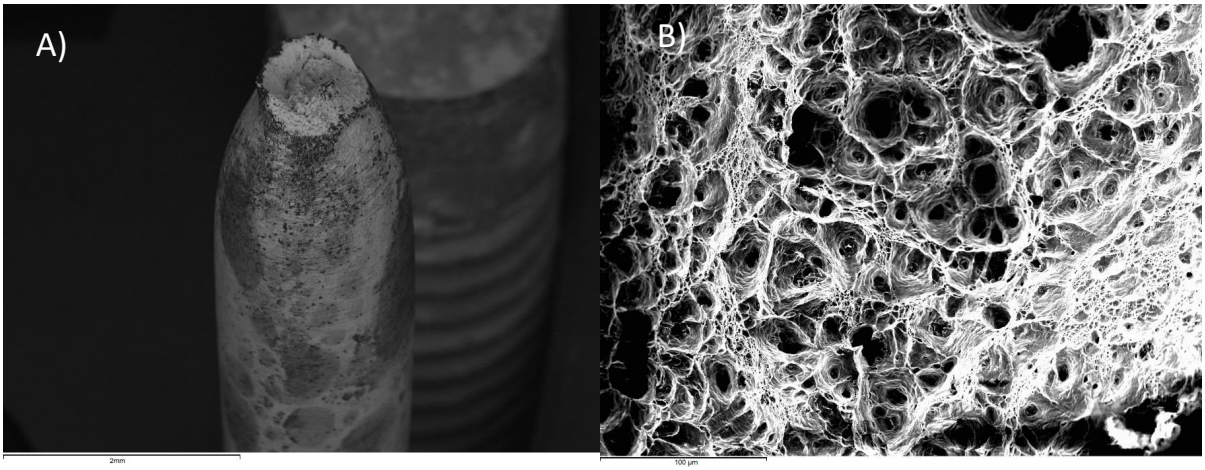

Figure 4.4.2: SEM images of FeCrAl sample broken in 1 wt% A) side view B)Surface view

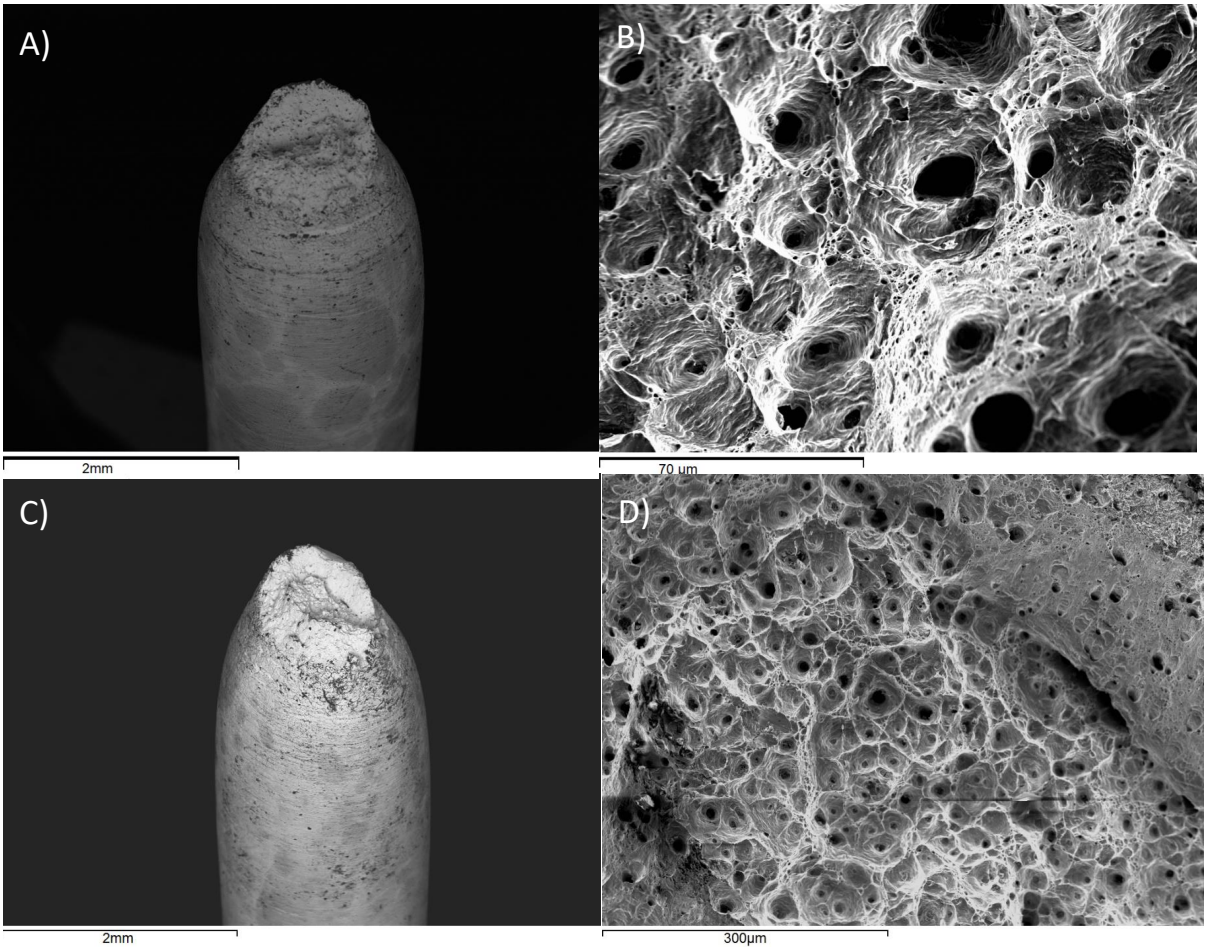

Figure 4.4.3: SEM images of FeCrAl samples broken in 5 wt% and 14 wt% bismuth A) 5 wt% side view B) 5 wt% surface view C) 14 wt% side view D) 14 wt% surface view

From previous experiments conducted in this study in LBE, the decrease in total elongation to failure down to 20% should indicate a mixture of ductile and brittle characteristics in the breaking mode of the sample. There was a fluctuation around 20% total elongation for the samples from 5 wt% to 14 wt% bismuth in the lead mixture. The SEM images of the samples drawn in 5 wt% and 14 wt% bismuth content in the lead mixture are shown in figure 4.4.3. As seen from the side view of both the samples in figure 4.4.3A, C show the strong neck formation again, which indicates the plastic deformation of the sample after the UTS. The fracture surface shown in figure 4.4.3B, D shows the characteristic ductile breaking mode with the dimple formation. Across the whole surface, there was only dimple formation and no evidence of a mix of ductile and brittle breaking modes. All samples between 5 wt% and 14 wt% bismuth in the lead had these similar features of strong necking characteristics and only dimple formation on the fracture surface. This means that the total elongation to failure is not indicative by itself of the ductility of the sample since in LBE, this total elongation was already causing brittle characteristics in the fracture modes present on the sample, while in lower content lead-bismuth the samples are still fully ductile. The lack of a gradual reduction in the total elongation to failure during this increase in bismuth content suggests that the active metal in the embrittlement process of these mixtures is still the lead and that the bismuth is not a significant concentration to cause LME. The second discrete level of bismuth when the ductility drops even further after the stable region is at 15 wt%. At this bismuth content, the total elongation to failure reduces from 19% to 18%, dropping the total elongation to failure below 19% for the first time.

The SEM images of the FeCrAl sample that was drawn in a 17.5 wt% bismuth-lead mixture are given in figure 4.4.4. The side profile of the FeCrAl sample, in figure 4.4.4A, shows a weaker neck formation than that of the previous samples at lower bismuth content. This, along with the reduction in the total elongation to failure, indicates that there is a reduction in the ductility of the sample at this bismuth content. The sample is not fully brittle at this bismuth content. From the surface image shown in figure 4.4.4B, there is a mix of brittle and ductile fracture modes in the sample. The middle of the sample still has the characteristic dimple formation. The two crack initiation sites shown in figure 4.4.4C, D on opposite sides of the sample depicts the brittle nature of the crack initiation.

Alternatively, it was at these conditions that the sample broken at 17.5 wt% was affected

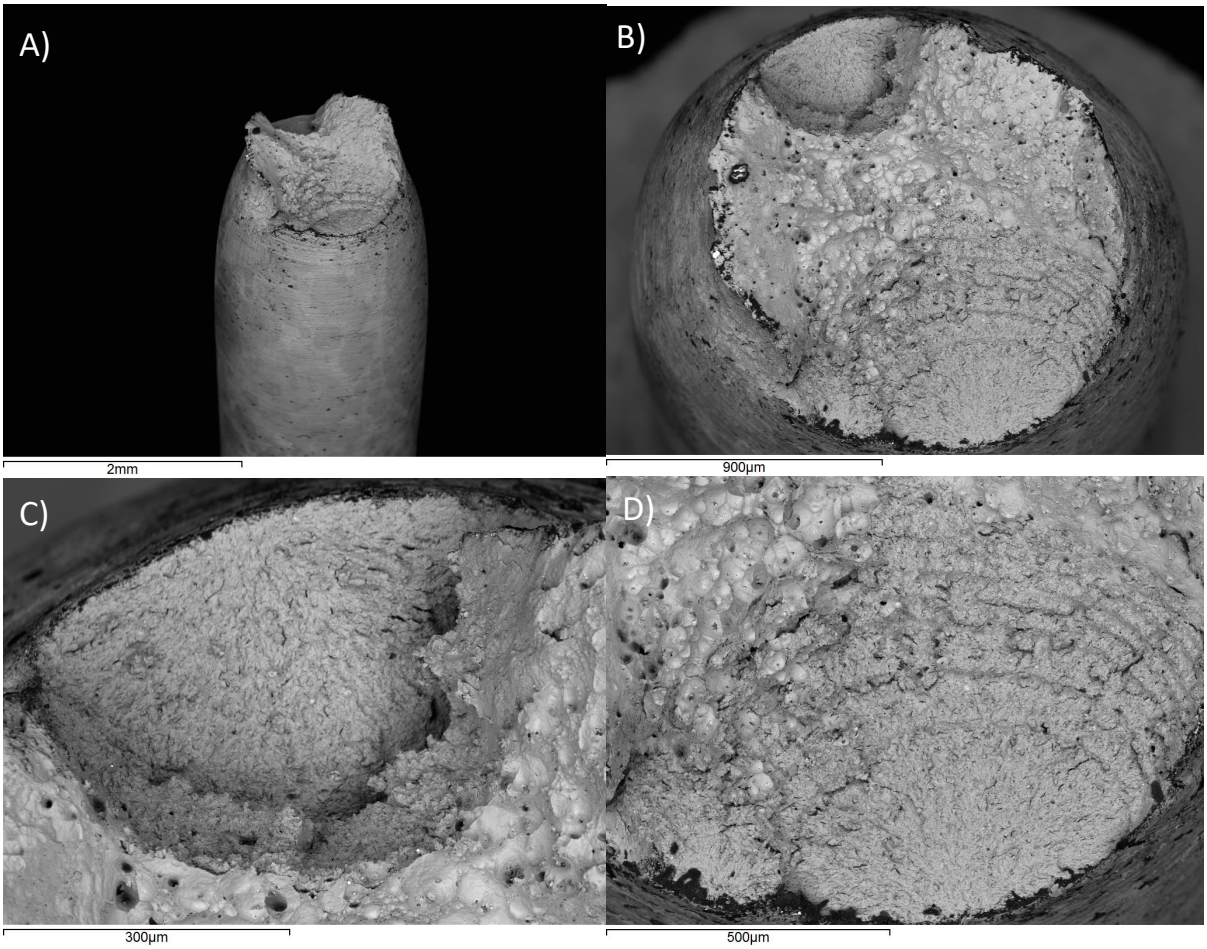

Figure 4.4.4: SEM images of FeCrAl sample broken in 17.5 wt% bismuth A) Side view B) Surface view C) Crack initiation site at the top of image B D) Crack initiation site at the bottom of image B

by LME which is why there is a brittle crack initiation. However, when the sample broke at the two crack initiation sites the strain rate significantly increased. This would have been due to the reduction in the gauge length. The equation for the gauge length is given as:

$$L_0 = k * \sqrt{A_0} \tag{4.1}$$

where L_0 is the gauge length, k is a constant either 5.65 or 5 according to EN specification or the ASME codes respectively, and A_0 is the cross-sectional area [61]. Since strain = $\Delta L/L$, where L is the gauge length, any elongation after the brittle crack initiation would have a more significant impact on the strain. Therefore, the strain rate increases after the initial crack formation. As seen in previous work an increase in the strain rate decreases the effect of LME [52, 54].

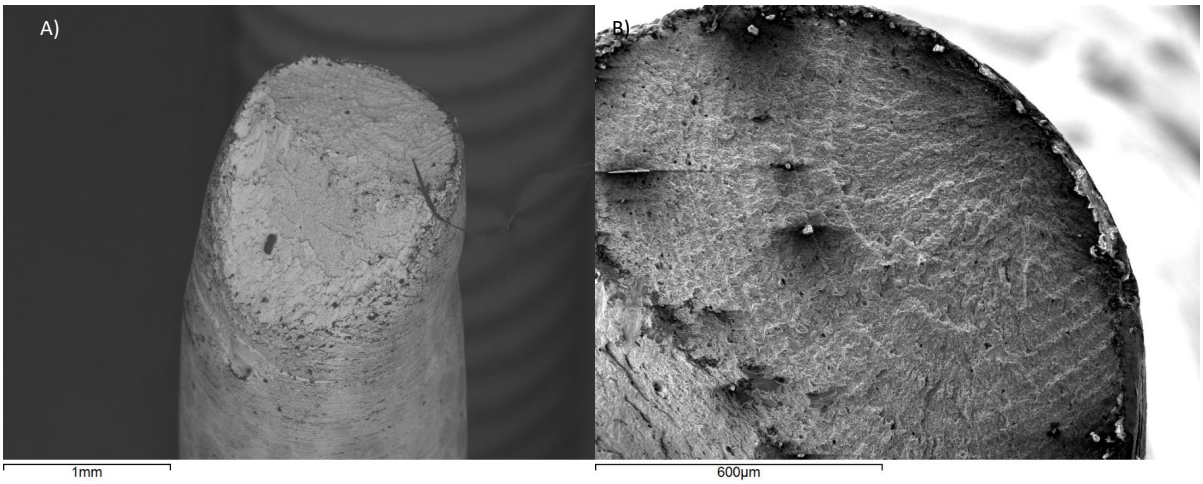

Figure 4.4.5: SEM images of FeCrAl sample broken in 30 wt% bismuth A) Side view B) Surface view

The SEM images of the FeCrAl sample that was broken in a 30 wt% bismuth-lead mixture are given in figure 4.4.5. The side profile of the sample, in figure 4.4.5A, depicts very minimal neck formation, suggesting that the sample broke shortly after the UTS was reached. The surface view of the sample, in figure 4.4.5B, shows the crack initiation site which has jagged cracks across the surface indicative of a intergranual and transgranular cracks typical in a brittle break. The SEM images along with the the total reduction of the elongation to failure value indicates that at this point the sample has been affected by LME.

Chapter 5

Discussion

5.1 LME Dependency on Temperature

The FeCrAl samples showed no reduction in elongation in liquid lead but did show a reduction in elongation in LBE, suggesting that the FeCrAl does not embrittle due to LME in liquid lead but does in LBE. The elongation to final breaking is plotted as a function of temperature to show the characteristic ductility trough that occurs due to LME as seen in figure 5.1.1.

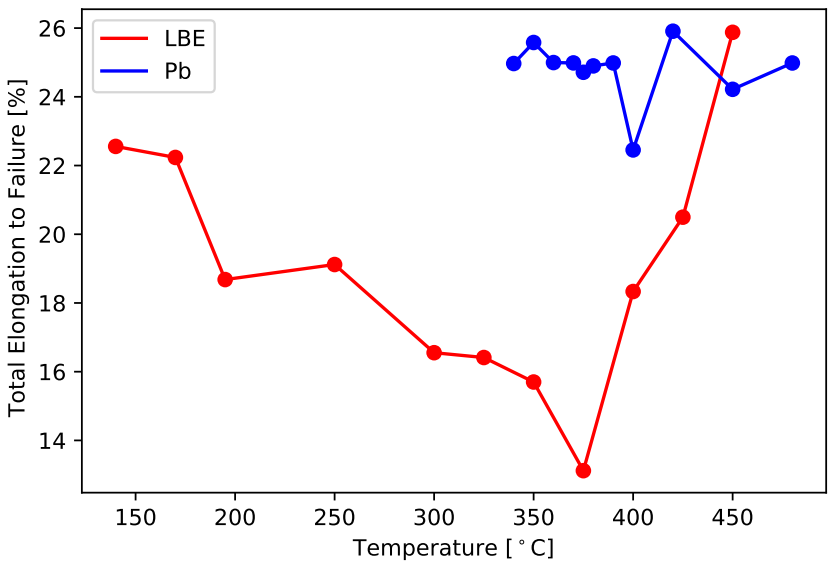

Figure 5.1.1: The elongation to failure as a function of temperature in both lead and LBE showing the ductility trough in the LBE environment

The figure clearly shows a reduction in the ductility for the LBE temperature series

between 250-400°C, with the strongest LME effect at 375°C. This temperature region is referred to as the ductility trough. There is a recovery of ductility above 400°C. The recovery of the ductility at elevated temperature is a common phenomenon when investigating LME. The exact cause for the recovery is not fully understood, though it may be that the rate of adsorption of the liquid metal atom is reduced at higher temperatures, therefore, the liquid metal atom does not reduce the intermetallic bond strength of the steel according to the adsorption induced reduction in cohesion model. Alternatively, the elevated temperature might increase the diffusion rate in the solid to a threshold where the obstacles to dislocation motion, which cause stress concentrators that trigger the brittle break, no longer build-up. A previous study that investigated a Fe-10Cr-4Al steel, similar in a macroscopic composition to the one developed at Kanthal, found that the recovery in ductility only occurred at 500°C in an LBE environment [57]. The difference in the recovery of ductility temperature is not exactly clear and may have to do with the differences in the reactive elements present in each type of FeCrAl alloy and carbon content of the steel, as these both have a significant influence on the oxide scale formation on the alloy. The 10-4 FeCrAl steel investigated in this report has been developed for the primary purpose of deployment in a liquid lead environment. The blend of reactive elements has been optimized to promote the formation of the alumina layer at a wide temperature range to prevent corrosion of the sample [25, 28, 29, 62]. The alloys are submerged in oxygen-depleted LBE in both cases, therefore the oxide scale properties are not as relevant in the discussion. Therefore, the differences with the reactive elements and impurities could result in different grain-size which leads to different behaviour in response to LME. The SEM images of the samples broken in liquid LBE, shown in figure 4.3.2, support this notion of the ductility trough. The samples broken at 140°C and at 425°C both show ductile characteristics in both the necking formation and the dimpled fracture surface. Whereas, the sample broken at 300°C and 350°C show brittle characteristics with no neck formation and brittle cracking modes on the sample surface.

In liquid lead, on the other hand, there was no evidence for LME despite other steels, such as T91, having shown strong susceptibility to LME in both stagnant LBE and stagnant lead [54, 55]. The SEM images of the side view and the surface of the samples broken in pure lead at 350°C and 375°C, depicted in figure 4.2.2, show ductile characteristics in the break. At these temperatures in LBE, the samples were completely brittle in fracture modes as evidenced by the SEM images. However, the

samples in pure lead did not demonstrate any effect from the LME. A major difference between the T91 ferritic/martensitic and the ferritic 10-4 FeCrAl is the oxide layer formed on the steel being chromia or alumina, respectively. As previously mentioned in section 2.1.2 the diffusion of the aluminum from the bulk of the metal is faster than that of the chromium [27]. Despite the test environment being oxygen free it is safe to presume that an oxide may still be present after the 24 hour wetting period. Due to the higher diffusion rate of aluminum to the surface zone it is possible to repair an oxide nano-layer on the newly exposed steel as the sample was drawn apart. This thin layer of alumina oxide would create enough of a barrier between the steel and the liquid metal. The oxide layer would inhibit an intimate contact between the liquid metal and steel and therefore the oxide would inhibit LME [53]. These results indicate that while the sample was affected by LME in LBE, pure lead did not seem to affect the FeCrAl, which shows promising results for the future application in the pure lead environment of an LFR.

5.2 LME Dependency on Bismuth

The reason for LBE causing LME and pure lead not causing LME in this FeCrAl steel is not fully understood, and may be a result of rapid oxide formation at the crack initiation sites preventing intimate contact between the steel and liquid metal. While there have been multiple models of LME presented in section 2.3.1, such as stress associated dissolution, the liquid metal weakening the intermetallic bonds at the crack tip in the solid metal, formation of micro-nano void ahead of the crack tip. The information gained from these models is not enough to rationalize why the FeCrAl steel is embrittled by LME in LBE but not in pure lead. As mentioned previously, a low mutual solubility between the solid and liquid couple promotes LME and a strong intermetallic bond inhibit LME, suggesting, a low chemical affinity between the solid-liquid couple. This would suggest that a similar electronegativity would inhibit LME, as these species would have a higher chemical affinity to one another. On the contrary, the observed correlation between LME and electronegativity is that a lower electronegativity difference promotes the occurrence of LME [63]. It has been reported that the chemical prerequisites for the active liquid metal and the solid metal to be embrittled by LME is that the two species should have a small difference in electronegativity as well as the previous requirements mentioned in section 2.3 of

limited mutual solubility, weak intermetallic bond strength, and good wettability. For the FeCrAl liquid lead couple, the active liquid metal is straightforward as this is a pure metal. For the FeCrAl LBE couple bismuth can be considered the active metal. The electronegativity of the steel will be considered as iron as this is the largest constituent of the FeCrAl, which is 1.83 on the Pauling Scale of electronegativity. The lead has an electronegativity of 2.33 and the bismuth has an electronegativity of 2.02. The bismuth and the steel have a smaller electronegativity difference than the lead and the steel, which may be a contributing factor in the LME effect observable in LBE but not pure lead. Previous experiments have determined that pure lead, pure bismuth, and LBE have different embrittlement effects. The severity of the embrittlement of T91 steel in these three liquid metal environments can be ranked from strongest to weakest as LBE, pure bismuth, and lead [54]. These results were gathered in oxygen saturated environments and, therefore, may not be able to be extrapolated to these conditions, however it does indicate that lead does not cause LME as severely as LBE.

Alternatively, the solubility limit of all alloying elements in the FeCrAl steel is at least one to two orders of magnitude greater in LBE than pure lead meaning that the corrosion effect is significantly greater in LBE [64]. While LME is not dissolution controlled process, the greater dissolution rate of the alloying elements could affect the may affect the oxide layer repair. Chromium is particularly affected by the transition from lead to LBE. Chromium's solubility limit increases 500 fold [64]. With chromia formation kinetically more favorable than alumina and acting as the nucleation site for the alumina formation [27], it is possible that the elevated dissolution rate of chromium is enough to prevent the oxide nano-layer formation. Without the protective oxide layer the LBE would be in intimate contact with the steel allowing for the LME phenomenon to occur.

The FeCrAl samples initially did not show a reduction in ductility until about 5 weight percent bismuth and a further reduction in ductility at about 15 weight percent bismuth. The elongation to final breaking is plotted as a function of the weight percent of bismuth in the lead-bismuth mixture shown in figure 5.2.1. The samples below 5 weight percent bismuth all have an elongation to failure of around 25% elongation, which suggests that these samples are fully ductile as they have a similar elongation as the samples drawn in pure lead, which have already been seen to be ductile. At 5 weight percent, there is a reduction in the total elongation to failure at around 20%. As seen from the samples in LBE, around 20% was a transition from fully ductile to

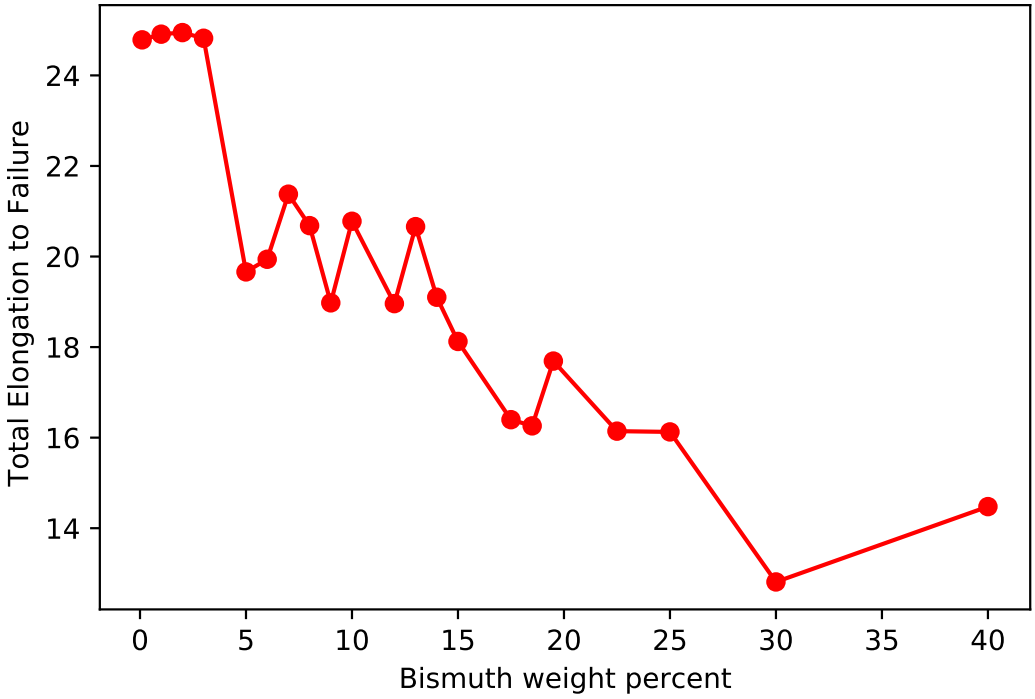

Figure 5.2.1: The elongation to failure as a function of increasing bismuth content

some ductile characteristics. That suggests that these samples should also have some ductile and some brittle characteristics. The total elongation to failure fluctuates for each sample around 20% until about 15 weight percent bismuth where it dropped to 18%. From 17.5wt% to 25wt% the total elongation to failure fluctuates around 16%. At 30wt% bismuth in the lead-bismuth melt the sample had another major reduction in ductility down to around 13%. At this point the sample was strongly affected by LME and exhibited brittle breaking modes, as seen in figure 4.4.5. This suggests a discrete effect rather than a continuous effect with the amount of bismuth in the lead-bismuth mixture.

The result of the crack tips becoming embrittled in a 17.5 wt% bismuth-lead environment, suggest that there is enough bismuth to cause LME at the surface, however, the bismuth content is not substantial enough for the diffusion of bismuth to the crack tip. According to the adsorption-induced reduction in cohesion model there needs to be a constant supply of the embrittling metal, which has been determined to be bismuth. Therefore the embrittlement is limited by the diffusion of bismuth to the crack tip which at the this content is too low to efficiently embrittle the center of the sample. It is only at 30wt% that there is enough bismuth present to ensure a constant

supply of bismuth to the crack tip, which causes the brittle break throughout the sample rather than just at the solid-liquid interface. This suggests that bismuth is the active metal in the embrittlement process for the 10-4 FeCrAl tested in this study.

Chapter 6

Conclusions

The Fe-10Cr-4Al ferritic steel samples in the oxygen-depleted pure lead did not show any LME effect during the SSRT experiments. These results are unexpected as ferritic steels tend to be more susceptible to LME. While there was severe LME in LBE. In the LBE environment there was a ductility trough resulting in the FeCrAl to show signs of embrittlement from 200°C to 400°C before ductility was recovered at 425°C. The most severe case of LME was in the LBE environment at 375°C. The YS and UTS were unaffected by the LME in all environments and testing conditions. From the evidence it was suggested that bismuth was the active embrittling element. At low concentrations of bismuth there was no occurrence of LME. At 5wt% bismuth there was the first reduction in ductility of the FeCrAl and only at 15 wt% is the bismuth content enough to cause embrittlement at the crack tip, however, the content was still not sufficient to cause LME throughout the whole sample. At 30 wt% the FeCrAl sample was fully embrittled throughout the break. The alumina also has some beneficial characteristic that prevents LME in pure lead. This positive effect, however, is not significant enough to eliminate LME the more corrosive environment of LBE. Further tests in pure bismuth would foundational in understanding if bismuth is the active element or if the binary eutectic system is more significant as a contributing factor to LME. Addtionally, conducting the tests in a flowing lead environment would be beneficial as this is the main parameter where a conservative approach was not taken. In an LFR lead would be flowing through the system at around 2 m/s which would cause erosion of the steel components. If the intimate contact between the lead and the steel was inhibited by an oxide layer on the FeCrAl then erosion of the oxide layer would have significant impact on the susceptibility of LME.

These results are promising for the usage of the 10-4 FeCrAl developed by Kanthal for load-bearing parts in an LFR, such as the fuel rods and heat exchangers, reducing the risk of premature failure. Further tests need to be conducted on the radiation tolerance of these steels. The swelling of the steel is likely not a substantial concern as ferritic steels are more resistant to radiation swelling than austenitic steels. The ferritic steels usually suffer from irradiation embrittlement. The high displacement per atom (DPA) values in a fast reactor – up to 200 DPA – may cause the ferritic steel to become brittle as the ductile to brittle transition temperature increases with irradiation. This needs to be thoroughly investigated before the potential application of these FeCrAl steels in LFR.

Bibliography

[1] *COP26 Outcomes*. en-GB. URL: https://ukcop26.org/the-conference/cop26-outcomes/ (visited on 02/01/2022).

[2] *World | Total including LUCF | Greenhouse Gas (GHG) Emissions | Climate Watch*. URL: https://www.climatewatchdata.org/ghg-emissions (visited on 02/02/2022).

[3] *Plans for New Nuclear Reactors Worldwide - World Nuclear Association*. URL: https://world-nuclear.org/information-library/current-and-future-generation/plans-for-new-reactors-worldwide.aspx (visited on 02/08/2022).

[4] Doligez, Xavier, Bouneau, Sandra, David, Sylvain, Ernoult, Marc, Zakari-Issoufou, Abdoul-Aziz, Thiollière, Nicolas, Bidaud, Adrien, Méplan, Olivier, Nuttin, Alexis, and Capellan, Nicolas. "Fundamentals of reactor physics with a view to the (possible) futures of nuclear energy". en. In: *Comptes Rendus Physique*. Demain l'énergie 18.7 (Sept. 2017), pp. 372–380. ISSN: 1631-0705. DOI: 10.1016/j.crhy.2017.10.004. URL: https://www.sciencedirect.com/science/article/pii/S1631070517300725 (visited on 02/08/2022).

[5] Markandya, Anil and Wilkinson, Paul. "Electricity generation and health". en. In: *The Lancet* 370.9591 (Sept. 2007), pp. 979–990. ISSN: 0140-6736. DOI: 10.1016/S0140-6736(07)61253-7. URL: https://www.sciencedirect.com/science/article/pii/S0140673607612537 (visited on 02/08/2022).

[6] *Death rates from energy production per TWh*. URL: https://ourworldindata.org/grapher/death-rates-from-energy-production-per-twh (visited on 02/08/2022).

[7] Gerasimov, A.S., Zaritskaya, T.S., Kiselev, G.V., and Myrtsymova, L.A. *BEHAVIOR OF RADIOTOXICITY AND DECAY HEAT POWER OF SPENT NUCLEAR FUEL OF VVER TYPE REACTORS AT LONG-TERM STORAGE*. FR0104395. 25, B.Cheremushkinskaya, Moscow, 117259, Russia: State Scientific Center of the Russian Federation Institute of Theoretical and Experimental Physics, Dec. 20, 2005, p. 4.

[8] *Home - Generation IV Goals*. GIF Portal. URL: https://www.gen-4.org/gif/jcms/c_9502/generation-iv-goals (visited on 02/09/2022).

[9] Diven, B. C., Terrell, J., and Hemmendinger, A. "Capture-to-Fission Ratios for Fast Neutrons in U^{235}". In: *Phys. Rev.* 109 (1 Jan. 1958), pp. 144–150. DOI: 10.1103/PhysRev.109.144. URL: https://link.aps.org/doi/10.1103/PhysRev.109.144.

[10] *UK selects HTGR for advanced reactor demonstration : New Nuclear - World Nuclear News*. URL: https://www.world-nuclear-news.org/Articles/UK-selects-HTGR-for-advanced-reactor-demonstration (visited on 02/27/2022).

[11] Media, TerraPower. *U.S. Department of Energy Awards TerraPower $80 Million to Demonstrate Advanced Nuclear Technology*. TerraPower. Oct. 14, 2020. URL: https://www.terrapower.com/doe-natrium-demonstration-award/ (visited on 02/27/2022).

[12] *Joint venture formed to spur SMR deployment in Sweden : New Nuclear - World Nuclear News*. URL: https://www.world-nuclear-news.org/Articles/Joint-venture-formed-to-spur-SMR-deployment-in-Swe (visited on 02/27/2022).

[13] Dehlin, Fredrik, Wallenius, Janne, and Bortot, Sara. "An analytic approach to the design of passively safe lead-cooled reactors". en. In: *Annals of Nuclear Energy* 169 (May 2022), p. 108971. ISSN: 0306-4549. DOI: 10.1016/j.anucene.2022.108971. URL: https://www.sciencedirect.com/science/article/pii/S0306454922000068 (visited on 02/28/2022).

[14] Toshinsky, G. I., Dedul, A. V., Komlev, O. G., Kondaurov, A. V., and Petrochenko, V. V. "Lead-Bismuth and Lead as Coolants for Fast Reactors". en. In: *World Journal of Nuclear Science and Technology* 10.02 (Feb. 2020). Number: 02 Publisher: Scientific Research Publishing, p. 65. DOI: 10.4236/wjnst.2020.

102007. URL: http://www.scirp.org/journal/Paperabs.aspx?PaperID=98300 (visited on 06/14/2022).

[15] Duchenko, O. V. and Dybkov, V. I. “Determination of NiBi3 reaction-diffusion constants in Ni-Bi couples”. en. In: *Journal of Materials Science Letters* 14.24 (Jan. 1995), pp. 1725–1727. ISSN: 1573-4811. DOI: 10.1007/BF00270989. URL: https://doi.org/10.1007/BF00270989 (visited on 06/14/2022).

[16] Aerts, Alexander. “Thermochemistry of Polonium Evaporation from LBE”. en. In: *Thermo* 1.2 (Sept. 2021), pp. 251–261. ISSN: 2673-7264. DOI: 10.3390/thermo1020017. URL: https://www.mdpi.com/2673-7264/1/2/17 (visited on 06/14/2022).

[17] *Handbook on Lead-bismuth Eutectic Alloy and Lead Properties, Materials Compatibility, Thermalhydraulics and Technologies*. English. NEA. 7268. OEDC & NEA, 2015, p. 950.

[18] Gardner, Leroy. “The use of stainless steel in structures”. en. In: *Progress in Structural Engineering and Materials* 7.2 (2005). _eprint: https://onlinelibrary.wiley.com/doi/pdf/10.1002/pse.190, pp. 45–55. ISSN: 1528-2716. DOI: 10.1002/pse.190. URL: https://onlinelibrary.wiley.com/doi/abs/10.1002/pse.190 (visited on 02/21/2022).

[19] Guo, Xianglong, Chen, Kai, Gao, Wenhua, Shen, Zhao, and Zhang, Lefu. “Corrosion behavior of alumina-forming and oxide dispersion strengthened austenitic 316 stainless steel in supercritical water”. en. In: *Corrosion Science* 138 (July 2018), pp. 297–306. ISSN: 0010-938X. DOI: 10.1016/j.corsci.2018.04.026. URL: https://www.sciencedirect.com/science/article/pii/S0010938X16311842 (visited on 02/21/2022).

[20] Huntz, A. M., Balmain, J., Tsaï, S. C., Messaoudi, K., Loudjani, M. K., Lesage, B., and Li, J. “Diffusion studies in oxides scales grown on alumina-and chromia-forming alloys”. en. In: *Scripta Materialia* 37.5 (Sept. 1997), pp. 651–660. ISSN: 1359-6462. DOI: 10.1016/S1359-6462(97)00167-X. URL: https://www.sciencedirect.com/science/article/pii/S135964629700167X (visited on 02/21/2022).

[21] Le Gall, M., Huntz, A. M., Lesage, B., Monty, C., and Bernardini, J. “Self-diffusion in α-Al2O3 and growth rate of alumina scales formed by oxidation: effect of Y2O3 doping”. en. In: *Journal of Materials Science* 30.1 (Jan. 1995),

pp. 201–211. ISSN: 1573-4803. DOI: 10.1007/BF00352151. URL: https://doi.org/10.1007/BF00352151 (visited on 02/21/2022).

[22] Yamamoto, Y., Brady, M. P., Lu, Z. P., Maziasz, P. J., Liu, C. T., Pint, B. A., More, K. L., Meyer, H. M., and Payzant, E. A. "Creep-Resistant, Al2O3-Forming Austenitic Stainless Steels". In: *Science* 316.5823 (Apr. 2007). Publisher: American Association for the Advancement of Science, pp. 433–436. DOI: 10.1126/science.1137711. URL: https://www.science.org/doi/10.1126/science.1137711 (visited on 02/23/2022).

[23] Brady, M. P., Yamamoto, Y., Santella, M. L., and Walker, L. R. "Composition, Microstructure, and Water Vapor Effects on Internal/External Oxidation of Alumina-Forming Austenitic Stainless Steels". en. In: *Oxidation of Metals* 72.5 (July 2009), p. 311. ISSN: 1573-4889. DOI: 10.1007/s11085-009-9161-2. URL: https://doi.org/10.1007/s11085-009-9161-2 (visited on 02/23/2022).

[24] Muralidharan, Govindarajan, Yamamoto, Y., Brady, M.P., Pint, Bruce, Voke, D., and Pankiw, R.I. "Development of cast alumina-forming Austenitic stainless steel alloys for use in high temperature process environments". In: *NACE - International Corrosion Conference Series* 2015 (Jan. 2015).

[25] Ejenstam, Jesper and Szakálos, Peter. "Long term corrosion resistance of alumina forming austenitic stainless steels in liquid lead". en. In: *Journal of Nuclear Materials* 461 (June 2015), pp. 164–170. ISSN: 0022-3115. DOI: 10.1016/j.jnucmat.2015.03.011. URL: https://www.sciencedirect.com/science/article/pii/S0022311515001555 (visited on 02/23/2022).

[26] Prescott, R. and Graham, M. J. "The formation of aluminum oxide scales on high-temperature alloys". en. In: *Oxidation of Metals* 38.3 (Oct. 1992), pp. 233–254. ISSN: 1573-4889. DOI: 10.1007/BF00666913. URL: https://doi.org/10.1007/BF00666913 (visited on 03/01/2022).

[27] Airiskallio, E., Nurmi, E., Heinonen, M. H., Väyrynen, I. J., Kokko, K., Ropo, M., Punkkinen, M. P. J., Pitkänen, H., Alatalo, M., Kollár, J., Johansson, B., and Vitos, L. "Third element effect in the surface zone of Fe-Cr-Al alloys". In: *Phys. Rev. B* 81 (3 Jan. 2010), p. 033105. DOI: 10.1103/PhysRevB.81.033105. URL: https://link.aps.org/doi/10.1103/PhysRevB.81.033105.

[28] Ejenstam, Jesper, Thuvander, Mattias, Olsson, Pär, Rave, Fernando, and Szakalos, Peter. “Microstructural stability of Fe–Cr–Al alloys at 450–550°C”. en. In: *Journal of Nuclear Materials* 457 (Feb. 2015), pp. 291–297. ISSN: 0022-3115. DOI: 10.1016/j.jnucmat.2014.11.101. URL: https://www.sciencedirect.com/science/article/pii/S0022311514009052 (visited on 03/01/2022).

[29] Ejenstam, Jesper, Halvarsson, Mats, Weidow, Jonathan, Jönsson, Bo, and Szakalos, Peter. “Oxidation studies of Fe10CrAl–RE alloys exposed to Pb at 550°C for 10,000h”. en. In: *Journal of Nuclear Materials* 443.1 (Nov. 2013), pp. 161–170. ISSN: 0022-3115. DOI: 10.1016/j.jnucmat.2013.07.023. URL: https://www.sciencedirect.com/science/article/pii/S0022311513009112 (visited on 03/01/2022).

[30] Dömstedt, Peter, Lundberg, Mats, and Szakalos, Peter. “Corrosion Studies of Low-Alloyed FeCrAl Steels in Liquid Lead at 750 °C”. en. In: *Oxidation of Metals* 91.3 (Apr. 2019), pp. 511–524. ISSN: 1573-4889. DOI: 10.1007/s11085-019-09896-z. URL: https://doi.org/10.1007/s11085-019-09896-z (visited on 03/01/2022).

[31] Stringer, John. “The reactive element effect in high-temperature corrosion”. en. In: *Materials Science and Engineering: A*. Proceedings of the 2nd International symposium on High Temperature Corrosion of Advanced Materials and Coatings 120-121 (Nov. 1989), pp. 129–137. ISSN: 0921-5093. DOI: 10.1016/0921-5093(89)90730-2. URL: https://www.sciencedirect.com/science/article/pii/0921509389907302 (visited on 03/01/2022).

[32] Hou, Peggy Y. “The Reactive Element Effect – Past, Present and Future”. In: *High-Temperature Oxidation and Corrosion 2010*. Vol. 696. Materials Science Forum. Trans Tech Publications Ltd, Sept. 2011, pp. 39–44. DOI: 10.4028/www.scientific.net/MSF.696.39.

[33] Dömstedt, Peter, Lundberg, Mats, and Szakálos, Peter. “Corrosion studies of a low alloyed Fe–10Cr–4Al steel exposed in liquid Pb at very high temperatures”. en. In: *Journal of Nuclear Materials* 531 (Apr. 2020), p. 152022. ISSN: 0022-3115. DOI: 10.1016/j.jnucmat.2020.152022. URL: https://www.sciencedirect.com/science/article/pii/S0022311519314023 (visited on 03/01/2022).

[34] Vargel, Christian. “Chapter C.8 - Crevice corrosion”. en. In: *Corrosion of Aluminium (Second Edition)*. Ed. by Christian Vargel. Amsterdam: Elsevier, Jan. 2020, pp. 267–271. ISBN: 978-0-08-099925-8. DOI: 10.1016/B978-0-08-099925-8.00020-X. URL: https://www.sciencedirect.com/science/article/pii/B978008099925800020X (visited on 03/02/2022).

[35] Frankel, G. S. “Pitting Corrosion of Metals: A Review of the Critical Factors”. en. In: *Journal of The Electrochemical Society* 145.6 (June 1998). Publisher: IOP Publishing, p. 2186. ISSN: 1945-7111. DOI: 10.1149/1.1838615. URL: https://iopscience.iop.org/article/10.1149/1.1838615/meta (visited on 03/02/2022).

[36] Tait, William S. “Chapter 27 - Controlling Corrosion of Chemical Processing Equipment”. en. In: *Handbook of Environmental Degradation of Materials (Third Edition)*. Ed. by Myer Kutz. William Andrew Publishing, Jan. 2018, pp. 583–600. ISBN: 978-0-323-52472-8. DOI: 10.1016/B978-0-323-52472-8.00028-9. URL: https://www.sciencedirect.com/science/article/pii/B9780323524728000289 (visited on 03/02/2022).

[37] Zhang, Jinsuo. “A review of steel corrosion by liquid lead and lead–bismuth”. en. In: *Corrosion Science* 51.6 (June 2009), pp. 1207–1227. ISSN: 0010-938X. DOI: 10.1016/j.corsci.2009.03.013. URL: https://www.sciencedirect.com/science/article/pii/S0010938X09000936 (visited on 03/02/2022).

[38] Alden, T, Stevenson, D A, and Wulff, J. “SOLUBILITY OF NICKEL AND CHROMIUM IN MOLTEN LEAD”. In: *Trans. Met. Soc. AIME* Vol: 212, No. 1 (Feb. 1958). URL: https://www.osti.gov/biblio/4330681.

[39] Callister, William D. “Corrosion and Degradation of Materials”. English. In: *Materials Science and Engineering: SI version*. Ed. by David G. Rethwisch. 9th ed. John Wiley & Sons, 2020, pp. 673–718. ISBN: 978-1-119-45391-8.

[40] Müller, G, Schumacher, G, and Zimmermann, F. “Investigation on oxygen controlled liquid lead corrosion of surface treated steels”. en. In: *Journal of Nuclear Materials* 278.1 (Feb. 2000), pp. 85–95. ISSN: 0022-3115. DOI: 10.1016/S0022-3115(99)00211-1. URL: https://www.sciencedirect.com/science/article/pii/S0022311599002111 (visited on 03/07/2022).

[41] "High-temperature Corrosion". en. In: *Electrochemistry and Corrosion Science*. Ed. by Nestor Perez. Boston, MA: Springer US, 2004, pp. 301–338. ISBN: 978-1-4020-7860-6. DOI: 10.1007/1-4020-7860-9_10. URL: https://doi.org/10.1007/1-4020-7860-9_10 (visited on 03/07/2022).

[42] Kofstad, Per. *High temperature corrosion*. London ; New York : New York, NY, USA: Elsevier Applied Science ; Sole distributor in the USA and Canada, Elsevier Science Pub. Co, 1988. ISBN: 978-1-85166-154-1.

[43] Müller, G, Heinzel, A, Schumacher, G, and Weisenburger, A. "Control of oxygen concentration in liquid lead and lead–bismuth". en. In: *Journal of Nuclear Materials* 321.2 (Sept. 2003), pp. 256–262. ISSN: 0022-3115. DOI: 10.1016/S0022-3115(03)00250-2. URL: https://www.sciencedirect.com/science/article/pii/S0022311503002502 (visited on 03/07/2022).

[44] Commission), Joint Research Centre (European, Hojna, A., and Nilsson, K.-F. *Overview of mechanisms & models for liquid metal embrittlement and future directions*. eng. LU: Publications Office of the European Union, 2018. ISBN: 978-92-79-97249-2. URL: https://data.europa.eu/doi/10.2760/017392 (visited on 11/30/2021).

[45] "Liquid Metal Induced Embrittlement". en. In: *Corrosion: Fundamentals, Testing, and Protection*. Ed. by Stephen D. Cramer and Bernard S. Covino. ASM International, 2003, pp. 381–392. ISBN: 978-1-62708-182-5. DOI: 10.31399/asm.hb.v13a.a0003635. URL: https://dl.asminternational.org/books/book/46/chapter/545389/liquid-metal-induced-embrittlement (visited on 03/15/2022).

[46] Huang, Xi, Gong, Xing, Song, Min, Chen, Jiajun, Hu, Feiyu, Yin, Yuan, Xiao, Jun, Wang, Hui, Wang, Hao, Gong, Haoran, Deng, Yangbin, Pang, Bo, and Li, Yongchun. "Liquid metal embrittlement susceptibility of a high-entropy alloy exposed to oxygen-depleted liquid lead-bismuth eutectic at 250 and 350 °C". en. In: *Journal of Nuclear Materials* 528 (Jan. 2020), p. 151859. ISSN: 0022-3115. DOI: 10.1016/j.jnucmat.2019.151859. URL: https://www.sciencedirect.com/science/article/pii/S0022311519309663 (visited on 03/15/2022).

[47] Old, C. F. "Liquid metal embrittlement of nuclear materials". en. In: *Journal of Nuclear Materials* 92.1 (Aug. 1980), pp. 2–25. ISSN: 0022-3115. DOI: 10.1016/

0022-3115(80)90136-1. URL: https://www.sciencedirect.com/science/article/pii/0022311580901361 (visited on 03/15/2022).

[48] Rostoker, W. and MARKUS, H. *Embrittlement by Liquid Metals*. Reinhold Publishing Corporation, 1960. URL: https://books.google.se/books?id=y4P4MgEACAAJ.

[49] Westwood, A. R. C., Preece, C. M., and Kamdar, M. H. "CHAPTER 10 - ADSORPTION-INDUCED BRITTLE FRACTURE IN LIQUID-METAL ENVIRONMENTS". en. In: *Engineering Fundamentals and Environmental Effects*. Ed. by H. Liebowitz. Academic Press, Jan. 1971, pp. 589–644. ISBN: 978-0-12-449703-0. DOI: 10.1016/B978-0-12-449703-0.50015-1. URL: https://www.sciencedirect.com/science/article/pii/B9780124497030500151 (visited on 03/17/2022).

[50] Lynch, S. P. "Environmentally assisted cracking: Overview of evidence for an adsorption-induced localised-slip process". en. In: *Acta Metallurgica* 36.10 (Oct. 1988), pp. 2639–2661. ISSN: 0001-6160. DOI: 10.1016/0001-6160(88)90113-7. URL: https://www.sciencedirect.com/science/article/pii/0001616088901137 (visited on 03/17/2022).

[51] Lynch, S. P. "Metallographic contributions to understanding mechanisms of environmentally assisted cracking". en. In: *Metallography* 23.2 (Sept. 1989), pp. 147–171. ISSN: 0026-0800. DOI: 10.1016/0026-0800(89)90016-5. URL: https://www.sciencedirect.com/science/article/pii/0026080089900165 (visited on 03/17/2022).

[52] Hamouche-Hadjem, Zehoua, Auger, Thierry, Guillot, Ivan, and Gorse, Dominique. "Susceptibility to LME of 316L and T91 steels by LBE: Effect of strain rate". en. In: *Journal of Nuclear Materials*. Heavy Liquid Metal Cooled Reactors and Related Technologies 376.3 (June 2008), pp. 317–321. ISSN: 0022-3115. DOI: 10.1016/j.jnucmat.2008.02.031. URL: https://www.sciencedirect.com/science/article/pii/S0022311508000743 (visited on 03/21/2022).

[53] Gong, Xing, Chen, Jiajun, Hu, Feiyu, Xiang, Congying, Yu, Zhiyang, Xiao, Jun, Wang, Hui, Gong, Haoran, Wang, Hao, Liu, Chaohong, Deng, Yangbin, Pang, Bo, Huang, Xi, Li, Yongchun, and Yin, Yuan. "Liquid metal embrittlement of an Fe10Cr4Al ferritic alloy exposed to oxygen-depleted and -saturated

lead-bismuth eutectic at 350°C". en. In: *Corrosion Science* 165 (Apr. 2020), p. 108364. ISSN: 0010-938X. DOI: 10.1016/j.corsci.2019.108364. URL: https://www.sciencedirect.com/science/article/pii/S0010938X19316154 (visited on 03/21/2022).

[54] Proriol Serre, Ingrid and Vogt, Jean-Bernard. "Liquid metal embrittlement sensitivity of the T91 steel in lead, in bismuth and in lead-bismuth eutectic". en. In: *Journal of Nuclear Materials* 531 (Apr. 2020), p. 152021. ISSN: 0022-3115. DOI: 10.1016/j.jnucmat.2020.152021. URL: https://www.sciencedirect.com/science/article/pii/S0022311519315284 (visited on 03/21/2022).

[55] Gong, Xing, Marmy, Pierre, Qin, Ling, Verlinden, Bert, Wevers, Martine, and Seefeldt, Marc. "Temperature dependence of liquid metal embrittlement susceptibility of a modified 9Cr–1Mo steel under low cycle fatigue in lead–bismuth eutectic at 160–450 °C". en. In: *Journal of Nuclear Materials* 468 (Jan. 2016), pp. 289–298. ISSN: 0022-3115. DOI: 10.1016/j.jnucmat.2015.06.021. URL: https://www.sciencedirect.com/science/article/pii/S0022311515300465 (visited on 03/21/2022).

[56] Gong, Xing, Chen, Jiajun, Xiang, Congying, Yu, Zhiyang, Gong, Haoran, and Yin, Yuan. "A comparative study on liquid metal embrittlement susceptibility of three FeCrAl ferritic alloys in contact with liquid lead-bismuth eutectic at 350°C". en. In: *Corrosion Science* 183 (May 2021), p. 109346. ISSN: 0010-938X. DOI: 10.1016/j.corsci.2021.109346. URL: https://www.sciencedirect.com/science/article/pii/S0010938X21001128 (visited on 03/21/2022).

[57] Gong, Xing, Hu, Feiyu, Chen, Jiajun, Wang, Hui, Gong, Haoran, Xiao, Jun, Wang, Hao, Deng, Yangbin, Pang, Bo, Huang, Xi, Li, Yongchun, and Yin, Yuan. "Effect of temperature on liquid metal embrittlement susceptibility of an Fe10Cr4Al ferritic alloy in contact with stagnant lead-bismuth eutectic". en. In: *Journal of Nuclear Materials* 537 (Aug. 2020), p. 152196. ISSN: 0022-3115. DOI: 10.1016/j.jnucmat.2020.152196. URL: https://www.sciencedirect.com/science/article/pii/S0022311520302294 (visited on 11/30/2021).

[58] IAEA. *Advances in Small Modular Reactor Technology Developments*. Sept. 2020.

[59] *Thomson PC Series Precision Linear Actuators*. URL: https://www.thomsonlinear.com/en/products/precision-linear-actuators/pc-series (visited on 03/22/2022).

[60] *Oxygen Analyzer SGM5*. en. URL: https://www.zirox.de/en/products/analyzers/oxygen-analyzer-sgm5/ (visited on 03/22/2022).

[61] Gene, Mathers. *Mechanical Testing - Tensile Testing Part 1*. en-GB. URL: https://www.twi-global.com/technical-knowledge/job-knowledge/mechanical-testing-tensile-testing-part-1-069.aspx (visited on 06/23/2022).

[62] Ejenstam, Jesper, Jönsson, Bo, and Szakalos, Peter. "Optimizing the Oxidation Properties of FeCrAl Alloys at Low Temperatures". en. In: *Oxidation of Metals* 88.3 (Oct. 2017), pp. 361–370. ISSN: 1573-4889. DOI: 10.1007/s11085-017-9718-4. URL: https://doi.org/10.1007/s11085-017-9718-4 (visited on 06/16/2022).

[63] Kamdar, M. H. "Liquid Metal Embrittlement". en. In: *Treatise on Materials Science & Technology*. Ed. by C. L. Briant and S. K. Banerji. Vol. 25. Embrittlement of Engineering Alloys. Elsevier, Jan. 1983, pp. 361–459. DOI: 10.1016/B978-0-12-341825-8.50015-5. URL: https://www.sciencedirect.com/science/article/pii/B9780123418258500155 (visited on 04/06/2022).

[64] Balbaud-Célérier, Fanny, Courouau, Jean-Louis, Féron, Damien, Martinelli, Laure, and Rouillard, Fabien. "13 - Corrosion of structural materials by liquid metals used in fusion, fission, and spallation". en. In: *Nuclear Corrosion*. Ed. by Stefan Ritter. European Federation of Corrosion (EFC) Series. Woodhead Publishing, Jan. 2020, pp. 437–457. ISBN: 978-0-12-823719-9. DOI: 10.1016/B978-0-12-823719-9.00013-5. URL: https://www.sciencedirect.com/science/article/pii/B9780128237199000135 (visited on 06/13/2022).

Appendix - Contents

Appendix A

First Appendix

This is only slightly related to the rest of the report

Appendix B

Second Appendix

this is the information